In vitro study on apoptotic cell death by effective magnetic hyperthermia with chitosan-coated $MnFe_2O_4$

2016 Nanotechnology 27 115101

(http://iopscience.iop.org/0957-4484/27/11/115101)

IOP Publishing Nanotechnology
Nanotechnology 27 (2016) 115101 (21pp) doi:10.1088/0957-4484/27/11/115101

In vitro study on apoptotic cell death by effective magnetic hyperthermia with chitosan-coated $MnFe_2O_4$

Yunok Oh[1], Nohyun Lee[2], Hyun Wook Kang[1,3,4] and Junghwan Oh[1,3,4]

[1] Center for Marine-integrated Biotechnology program (BK21 Plus), Pukyong National University, Busan, 48547, Korea
[2] School of Advanced Materials Engineering, Kookmin University, Seoul, 02707, Korea
[3] Department of Biomedical Engineering; Pukyong National University, Busan, 48547, Korea
[4] Interdisciplinary Program of Biomedical Mechanical & Electrical Engineering, Pukyong National University, Busan, 48547, Korea

E-mail: wkang@pknu.ac.kr and jungoh@pknu.ac.kr

Received 11 August 2015, revised 31 December 2015
Accepted for publication 6 January 2016
Published 12 February 2016

Abstract

Magnetic nanoparticles (MNPs) have been widely investigated as a hyperthermic agent for cancer treatment. In this study, thermally responsive Chitosan-coated $MnFe_2O_4$ (Chitosan-$MnFe_2O_4$) nanoparticles were developed to conduct localized magnetic hyperthermia for cancer treatment. Hydrophobic $MnFe_2O_4$ nanoparticles were synthesized via thermal decomposition and modified with 2,3-dimercaptosuccinic acid (DMSA) for further conjugation of chitosan. Chitosan-$MnFe_2O_4$ nanoparticles exhibited high magnetization and excellent biocompatibility along with low cell cytotoxicity. During magnetic hyperthermia treatment (MHT) with Chitosan-$MnFe_2O_4$ on MDA-MB 231 cancer cells, the targeted therapeutic temperature was achieved by directly controlling the strength of the external AC magnetic fields. *In vitro* Chitosan-$MnFe_2O_4$-assisted MHT at 42 °C led to drastic and irreversible changes in cell morphology and eventual cellular death in association with the induction of apoptosis through heat dissipation from the excited magnetic nanoparticles. Therefore, the Chitosan-$MnFe_2O_4$ nanoparticles with high biocompatibility and thermal capability can be an effective nano-mediated agent for MHT on cancer.

Keywords: $MnFe_2O_4$ nanoparticles, magnetic hyperthermia, chitosan, cell death, apoptosis, cellular uptake

(Some figures may appear in colour only in the online journal)

1. Introduction

As a therapeutic agent, magnetic nanoparticles (MNPs) have received significant attention due to their unique physical and chemical features such as electronic, magnetic, and optical properties [1]. Ferrite nanoparticles including iron oxide nanoparticles in uniform size (⩽100 nm) have been used as a magnetic agent in various biomedical applications including magnetic resonance imaging (MRI) [2–5], diagnostic sensing [6–8], cancer hyperthermia [9–13], and drug delivery [14–17] on account of their magnetism and excellent biocompatibility. In particular, magnetic hyperthermia treatment (MHT) is one of the promising non-invasive approaches for thermal activation therapy on cancerous tumors. Upon exposure to external alternating current (AC) magnetic fields, MNPs can generate heat through the oscillation of their magnetic moments. MHT can then kill cancer cells by elevating their temperature to 42 ∼ 45 °C with minimal injury to normal cells, because the cancer cells are typically more vulnerable to hyperthermic temperatures (40 ∼ 45 °C) than the normal cells due to low O_2 and pH by insufficient blood perfusion. Therefore, in comparison to the conventional chemotherapy and radiotherapy on cancer, MHT associated with localized thermal energy can reduce severe side-effects on the normal cells [18, 19].

The therapeutic efficacy of MHT depends on the physical properties of MNPs and the frequency as well as the amplitude of the applied alternating current (AC) to generate magnetic fields. Since the conventional MHT systems typically have fixed operation settings, most of the recent research has focused primarily on a variety of synthesis and surface modifications of the MNPs to compensate for systemic limitations and to obtain high induction heating efficiency. Thus, the development of the optimal magnetic agents is quite instrumental to achieving effective hyperthermia performance with minimal MNP dose. Recently, the synthesis of efficient hyperthermia agents with high specific absorption rate (SAR) values was investigated in terms of the MNP size, shape, and core–shell components [20–22]. Although extensive studies have reported the modified MNPs with higher SAR values, further research on the biocompatibility of MNPs with high SAR values is still necessary to develop high-quality functionalized MNPs to enhance the therapeutic efficacy and safety of MHT.

Surface modifications of nanoparticles primarily determine the functional properties of MNPs such as the surface charge of the nanoparticles, risk of immunogenicity, and the degree of cellular uptake. Among various natural coating materials studied to date, chitosan has attracted considerable attention. As a deacetylated derivative of chitin, chitosan is a non-toxic biocompatible and biodegradable natural polymer, of which the positive surface charge can prevent agglomeration of the nanoparticles. In comparison with many other polymers, the chitosan backbone contains a number of free amine groups, allowing the binding of various agents. Thus, the presence of both reactive amino groups and hydroxyl groups on the chitosan enables further functionalization of the MNP surface for theranostic applications. In addition, due to its excellent biocompatibility, chitosan has been widely used in tissue engineering and nanomedicines [23–26]. Therefore, chitosan-coated MNPs can be a nano-therapeutic adjuvant for safe cancer hyperthermia. In our study, we fabricated $MnFe_2O_4$ nanoparticles modified with chitosan due to three advantages of MHT: first, achieving high magnetization designed by uniform bimetallic $MnFe_2O_4$ nanoparticles; second, improving biocompatibility and colloidal stability in aqueous media; finally, encapsulating an appropriate coating layer to minimize loss of magnetic property of the core and to facilitate further modifications on targeting agents, drugs, and oligonucleotides.

Although a number of researches have demonstrated the feasibility of cancer hyperthermia with the application of biocompatible chitosan-coated MNPs, few studies reported the optimal dosage and treatment conditions pertaining to the delayed cellular death induced by MHT. Besides, it is still difficult to deliver the optimal thermal energy to cancerous tumors due to the dependence of heat capacity on tumor characteristics such as type, stage, size, and hardness. Typically, cancer cells are more sensitive to mild heat ($40 \sim 45\,^{\circ}C$) than normal cells, in that compactly disorganized vasculature and reduced blood flow in a tumor hardly dissipates heat to the surrounding area [27–29]. Thus, the cancer cells treated by localized heat during hyperthermia undergo apoptosis, leading to cellular death. On the other hand, the application of higher temperatures ($\sim 52\,^{\circ}C$ or above) can directly kill or weaken both normal and cancerous cells throughout necrosis and can eventually cause chronic inflammation during the healing process. For effective apoptotic cancer hyperthermia without necrosis of normal cells, it is essential to sustain therapeutic heat primarily in the targeted tumor at the appropriate dose of nanoparticles. Therefore, the main objectives of the current study include: (1) synthesis of water-stable, biocompatible chitosan-coated $MnFe_2O_4$ nanoparticles with high SAR values; (2) continuous delivery of localized therapeutic temperature to the cancer cells under AC magnetic fields; and (3) *in vitro* investigations on apoptotic cell death post-MHT.

2. Experiments

2.1. Chemical materials

1,2-hexadecanediol (90%), oleic acid (90%), oleylamine (70%), iron(III) acetylacetonate ($Fe(acac)_3$), manganese(II) acetylacetonate ($Mn(acac)_2$), 1-octadecene (90%), chitosan (deacetylation 85%, Mw 50 KDa, viscosity $20 \sim 300$ (cP)), acetic acid and N-(3-Dimethylaminopropyl)-N′-20ethylcarbodiimide hydrochloride (EDC) were purchased from Sigma-Aldrich Co. (St. Louis, MO, USA). DMSA was purchased from TCI - Tokyo Chemical Industry Co., Ltd (Chuo-ku, Japan). Dimethyl sulfoxide (DMSO) and toluene were obtained from Junsei Chemical Co., Ltd (Tokyo, Japan). Absolute ethanol and n-hexane were purchased from Samchun Pure Chemical Co., Ltd (Pyeongtaek-si, Gyeonggi-do, Korea). Milli-Q water was used for all the aqueous solutions. All chemicals were of analytical grade reagents and used as received without further purification.

2.2. Preparation of chitosan-coated $MnFe_2O_4$ nanoparticles

2.2.1. Synthesis of $MnFe_2O_4$ nanoparticles. $MnFe_2O_4$ MNPs were synthesized through a standard procedure reported by Sun *et al* [30]. The synthesis was carried out using a standard Schlenk line technique. $Mn(acac)_2$ (1 mmol), $Fe(acac)_3$ (2 mmol), 1,2-hexadecanediol (10 mmol) and 1-octadecene (20 ml) were stirred and mixed under inert nitrogen. After oleic acid (6 mmol) and oleylamine were injected, the mixture was stirred at 100 °C for 30 min and then heated to 200 °C for 2 h. The solution was refluxed for 1 h at 320 °C at the heating rate of 3.3 °C/min with vigorous magnetic stirring. The resulting solution was cooled down to room temperature, and ethanol was added to the solution to precipitate the black materials, which were separated by centrifugation and re-dissolved in n-hexane.

2.2.2. Synthesis of biocompatible $MnFe_2O_4$ nanoparticles. Figure 1 illustrates a synthesis process for $MnFe_2O_4$ coated with chitosan. Due to coating with a layer of hydrophobic ligand oleate, the resulting $MnFe_2O_4$ was insoluble in aqueous solution. For biomedical application, the $MnFe_2O_4$

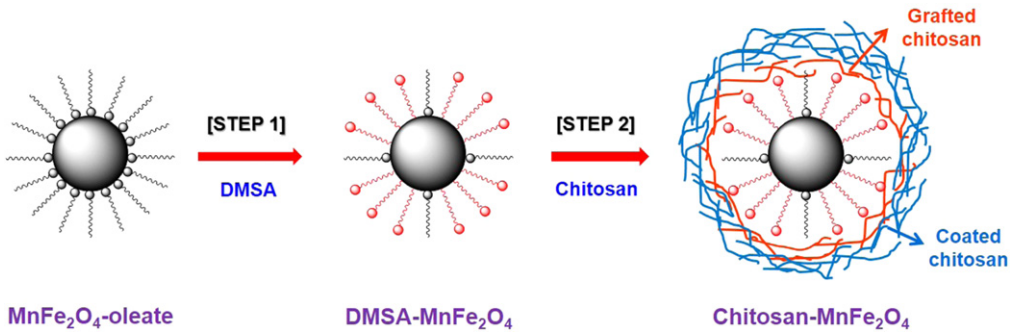

Figure 1. Schematic diagram of synthesis of Chitosan-$MnFe_2O_4$ nanoparticles.

nanoparticles were initially transferred to be hydrophilic by a ligand exchange reaction using DMSA and then conjugated with biocompatible chitosan [31]. $MnFe_2O_4$ nanoparticles (~10 mg) with the desired size were dissolved in 1 ml of toluene. 10 mg of DMSA were dissolved in 1 ml of DMSO, and the solution was then added into the nanoparticle solution with vigorous magnetic stirring. The mixed solution was stirred for 24 h at room temperature. The black precipitates were separated by centrifugation and purified by means of multiple purified water washes with a magnet. Then, the obtained DMSA-$MnFe_2O_4$ nanoparticles were redispersed in water. The chitosan-coated $MnFe_2O_4$ nanoparticles were prepared by cross-linking technique [32]. 3 ml of DMSA-$MnFe_2O_4$ nanoparticles in aqueous solution (10 mg ml^{-1}) were added to 5 ml (1 w/v%) of chitosan acetic aqueous solution. The mixed solution was sonicated while chitosan was electrostatically attached to the surface of the DMSA-$MnFe_2O_4$. After the addition of 2 ml of aqueous EDC solution (1.2 wt%), the mixed solution was sonicated for 4 h and reacted for 24 h at room temperature. As low molecular weight chitosan had poor solubility in water, 1 w/v% acetic aqueous solution was used for the coupling reaction between the EDC and carboxyl groups of the DMSA-$MnFe_2O_4$ nanoparticles to gain good colloidal stability without aggregation during the coupling reaction. Thus, an EDC-coupling reaction resulted in the formation of an amide bond between the positively charged amine of chitosan and the negatively charged carboxylic acid of the DMSA. Finally, the resulting product was washed three times with water by a permanent magnet. To remove some aggregated particles, the nanoparticle solution was filtered through a 0.2 μm syringe filter.

2.3. Characterization of MNPs

2.3.1. The structural characterization of MNPs. The crystal structure of the synthesized nanoparticles was analyzed with x-ray diffraction (XRD) (X'Pert-MPD System, Philips, Almelo, Netherlands). The chemical functional groups of the nanoparticles were monitored using a Fourier transform infrared spectroscopy (FTIR) spectrometer (FT/IR 6100, Jasco, Easton, Pennsylvania, USA).

2.3.2. The content of magnetic atoms. Both the organic and inorganic contents of the nanoparticles were measured with thermal gravimetric analysis (TGA) (TGA 7, Pyris 1, Perkin Elmer, Waltham, Massachusetts, USA). The TGA curves of the nanoparticles were measured under a nitrogen atmosphere from room temperature to 700 °C with a heating rate of 10 °C/min. The elemental analysis of the magnetic nanoparticles was evaluated by SEM/EDS (scanning electron microscope/energy dispersive x-ray spectroscopy) (Hitachi, S-2400, Japan/Kevex Ltd, Sigma) and LAM-ICP-MS (laser ablation microprobe-inductively coupled plasma mass spectrometry (Perkin Elmer, Elan DRC-e, UP-213, USA) analysis. The surface elemental compositions and impurities of the magnetic nanoparticles were identified using EDS analysis in a specific scan area on the SEM sample at 20 keV. EDS is helpful in identifying chemical composition on the surface of a variety of foreign materials. EDS analyzes the chemical composition of a sample by separating the characteristic x-rays of different elements into an energy spectrum. EDS spectroscopy as a histogram of the x-ray energy with individual peaks is proportional to the amount of a specific element analyzed. So, the EDS system can be employed for identifying elemental compositions within the sample. The fraction of magnetic atoms (Mn and Fe) in the magnetic nanoparticles was determined by ICP-MS. ICP-MS provides highly sensitive elemental analysis for the determination of multi-trace elements. To measure the final composition of magnetic atoms, the organic coating layer and residual ligands on magnetic nanoparticles were removed by annealing the samples in air at 450 °C for 4 h. And then the magnetic nanoparticles were dissolved in a 65% HNO_3 and 37% HCl (3:1) acid solution at 60 °C. The digested solution was diluted to a level of 1 to 5 ppm for the ICP-MS measurement.

2.3.3. Magnetic property of MNPs. The magnetic behavior (such as coercivity and saturation magnetization) of each of the magnetic nanoparticles was measured by a superconducting quantum interference device (SQUID) with a magnetic property measurement system (MPMS XL 7.0, Quantum Design, San Diego, CA, USA) at 300 K. ~0.035 g of the powder sample was used for measurement in the applied field from −4 to 4 T. The saturation magnetization (Ms) of the magnetic nanoparticles can be determined from a hysteresis curve. The Ms value of the $MnFe_2O_4$ magnetic core was calculated on the basis of TGA measurement according

to the following formula [33]

$$Ms = Ms^{MnFe_2O_4}\,(100 - \omega)$$

where $Ms^{MnFe_2O_4}$ is the saturation magnetization for the $MnFe_2O_4$ magnetic core and ω is the mass loss (%) calculated by TGA data. And finally, the Ms value corresponding to magnetic atoms (Mn and Fe) was normalized to the mass fraction of the magnetic atoms derived from ICP-MS.

2.3.4. Particle size and distribution. The average size and shape of the nanoparticles were determined by high resolution transmission electron microscopy (HR-TEM) (JEM 2010, JEOL Ltd, Tokyo, Japan). The mean size and distribution of the nanoparticles determined by TEM were calculated by measuring the diameter of about 100 nanoparticles with the corresponding histogram of particle size using image analysis software (Image J 1.49, NIH, USA). The average hydrodynamic size and polydispersity index of the nanoparticles were evaluated by a laser diffraction particle size analyzer (PSA) (Beckman Coulter, LS 13320, CA, USA). The surface charge of the nanoparticles was determined by zeta potential measurement (Beckman Coulter, LS 13320, CA, USA). To measure the broadness of a molecular weight distribution of the as-synthesized Chitosan-$MnFe_2O_4$ nanoparticles, the polydispersity index (PDI) was calculated, and is defined by: [34, 35]

$$PDI = \frac{D_w}{D_n}$$

Where PDI is the polydispersity index, D_n is the number-average diameter, D_w is the weight-average diameter.

2.4. Measurement of magnetically induced hyperthermic effect

To investigate magnetic heating efficiency, 1 ml of water-dispersed Chitosan-$MnFe_2O_4$ nanoparticles solution was displaced in a glass flat-bottomed cylindrical vial (diameter = 12 mm) as a sample holder under non-adiabatic apparatus. The sample concentration was 1.5 mg magnetic atoms/ml. The sample holder was subjected to an AC magnetic field of 0.6 Tesla, of which the field generator contained a 3-turn, 6 mm thick, and 65 mm of inner radius of copper coil equipped with an optical thermometer (AMOTH 8000, Anritsu Meter Co., Ltd, Japan). The optical thermometer was positioned at the center of the sample holder. The temperature differences according to the vertical and horizontal position of the optical thermometer in the sample holder appeared within ± 1 °C. Induction heating was then investigated as a function of the applied AC magnetic field amplitudes ranging from 20 to 60 kA m^{-1} at a fixed frequency of 307 kHz. The temperature of the sample solution was measured with a thermometer positioned at the center of the sample holder.

The heating ability of the magnetic materials in the presence of the AC field was expressed by SAR, which was defined as the power of heating magnetic material per unit g. SAR was determined by the initial linear increase in temperature (dT) per time interval (dt) as follows [29, 36–38]

$$SAR\ (W/g) = \frac{cmd}{mmag} \times \frac{dT}{dt}$$

where c (J/g · °C) is the specific heat capacity (i.e. J/g · °C), md the dispersion mass, $mmag$ (g/L) is the magnetic ion mass, and dT/dt is the maximal slope at initial times after applying the magnetic fields. Typically, SAR is dependent on the property (i.e. particle size, shape, distribution, and doped metal) and concentration of the nanoparticles as well as the applied AC magnetic fields for the hyperthermia application [39, 40]. To directly evaluate hyperthermal efficiency, the current study compared the SAR of Chitosan-$MnFe_2O_4$ nanoparticles with that of commercially available iron oxide nanoparticles, Feridex (FDA-approved) as a control at the same concentration of 1.5 mg magnetic atoms/ml under the AC field amplitude of 50 kA m^{-1} at 307 kHz.

2.4.1. Cell culture. MDA-MB-231 breast cancer cells (Korea Cell Line Bank, Seoul, Korea) were used and cultured in a monolayer in Dulbecco's Modified Eagle Medium (DMEM, Thermo Scientific, Waltham, MA, USA), which was supplemented with 10% fetal bovine serum (FBS, Thermo Scientific, Waltham, MA, USA). The cultured cells were incubated at 37 °C in humidified atmosphere of 5% CO_2 and 95% air, and the cell growth medium was changed twice a week. Then, the cells were harvested with a 0.025% trypsin-EDTA solution.

2.4.2. Cell viability assay. Prior to the hyperthermia experiments, the degree of cytotoxicity was assessed for the synthesized MNPs. MDA-MB 231 cells were seeded in a 96-well plate at a density of 1×10^4 cells/well in 100 μl of culture medium and incubated for 24 h. The different concentrations of the DMSA-$MnFe_2O_4$ and Chitosan-$MnFe_2O_4$ nanoparticles (0.1, 0.5, 1.0, and 1.5 mg ml^{-1}) were added into the culture medium. A water-soluble tetrazolium salts (WST-1, Roche Life Science, IN, USA) cytotoxicity assay was employed to examine the *in vitro* cytoxicity of Chitosan-$MnFe_2O_4$ nanoparticles on MDA-MB-231 cells. A well with no MNP sample was used as a control. The cells were cultured at 37 °C in a humidified 5%-CO_2 incubator to determine the effect of the incubation time (12, 24, and 48 h) on cell viability. After various times of incubation, 10 μl of WST-1 reagent was added to each well of the 96-well plate. Then, the plate was mixed gently side-to-side for one minute, and the cells with WST-1 were incubated for 2 h. After incubation, the 96-well plate was mixed gently for one minute to homogenize the color distribution. An ELISA micro-plate reader (SpectraMax 340, Molecular Device, Sunnyvale, CA, USA) measured the absorbance of each well at a wavelength of 450 nm. Cell viability was then

evaluated as the ratio of absorbance between the control and sample groups.

2.4.3. Cellular uptake. The cellular uptake of the Chitosan-$MnFe_2O_4$ nanoparticles was observed in the MDA-MB-231 cell using Prussian blue staining [41, 42] and was quantified by ICP-MS [43]. To evaluate the cellular uptake of the Chitosan-$MnFe_2O_4$ nanoparticles on the MDA-MB-231 breast cancer cells, the cells were seeded at a density of 2×10^5 cells/ml in a 1 ml medium in a 35 mm cell culture dish and incubated for 24 h. After 24 h incubation, Chitosan-$MnFe_2O_4$ nanoparticles (1.5 mg magnetic atoms/ml) were added into the 1 ml of culture medium and incubated for another 24, 48, and 72 h. For the Prussian blue stain, first, the cell dishes were fixed with cold 70% ethanol for 20 min and washed with distilled water. And then the cells were incubated with 10% potassium ferrocyanide and 20% aqueous solution of hydrochloric acid for 20 min, followed by a nuclear fast red (Sigma-Aldrich) counter stain. The cell morphology was observed using optical microscopy. For the quantitative analysis of the intracellular uptake of Chitosan-$MnFe_2O_4$ nanoparticles, the cells after incubation (24, 48, and 72 h) with the Chitosan-$MnFe_2O_4$ nanoparticles (1.5 mg magnetic atoms/ml) were trypsinized and collected by centrifugation. The collected cells were lysed by nitric acid and hydrochloric acid. The amount of the nanoparticles cell uptake was quantified using LAM-ICP-MS (Perkin Elmer, Elan DRC-e, UP-213, USA) and the resulting concentration was divided by counting the cell numbers.

2.4.4. In vitro MHT

2.4.4.1. Cancer hyperthermia. To investigate the hyperthermic effects of the Chitosan-$MnFe_2O_4$ nanoparticles on breast cancer cells *in vitro*, MDA-MB- 231 cells were seeded at a density of 2×10^5 cells/ml in a 35 mm culture dish of 1 ml medium. Initially, the temperature development was measured by a digital optical thermometer in the cells with MNPS (1.5 mg magnetic atoms/ml), and the schematic diagram for in vitro localized magnetic hyperthermia treatment is shown in figure 2. For a control, the magnetic field was applied at 50 kA m^{-1} to identify the maximum temperature in the cell culture dish. To achieve two hyperthermic temperatures of 42 and 52 °C, the applied magnetic field was adjusted from the initial amplitude of 50 kA m^{-1} to 20 and 35 kA m^{-1} respectively, once the required temperature was reached. Then, five different conditions were tested to explore the hyperthermic effects of the MNPs and MHT on the MDA-MB-231 cells: (1) untreated cells without MNPs and MHT (control), (2) cells treated with MNPS and without MHT (CM), (3) cells treated without NMPs and MHT and incubated at 42 °C for 30 min (HT-42), (4) cells treated with MNPs and MHT at 42 °C for 30 min (MHT-42), and (5) cells treated with MNPs and MHT at 52 °C for 30 min (MHT-52). Each sample was incubated at various times (0, 24, and 48 h). The concentration of Chitosan-$MnFe_2O_4$ nanoparticles was 1.5 mg magnetic atoms/ml. All the cells after each incubation time were imaged with an optical microscope (DMI300B, Leica, Germany) for direct comparison.

2.4.5. Apoptosis assay

2.4.5.1. Microscopic analysis. Changes in the cell morphology and populations were observed to evaluate the apoptosis-inducing effects of the Chitosan-$MnFe_2O_4$ nanoparticles on cancer cells at various recovery times of 0, 24, and 48 h after MHT. All the adherent cells were directly washed twice with cold PBS and once with a 1X binding buffer after *in vitro* MHT. For qualitative determination of the *in vitro* apoptosis, the washed cells were initially stained by an Annexin V-FITC Apoptosis Detection Kit (BD Biosciences, CA, USA) and Hoechst 33342 (Sigma-Aldrich Co, St. Louis, MO, USA) at the concentration of 10 μg ml^{-1} for 15 min at room temperature in a dark environment and evaluated by a fluorescence microscope (DMI300B, Leica, Wetzlar, Germany). The Annexin V-FITC apoptosis detection kit contains Annexin V-FITC (fluorescein) conjugate, propidium iodide (PI) solution. The Annexin V-FITC conjugate detects early apoptosis in green fluorescence after being bound to phosphatidylserine (PS), which is typically exposed during the early stage of apoptosis. The PI solution detects late apoptotic or necrotic cells in red fluorescence by permeating the membranes of the damaged and dead cells. Thus, live cells show no fluorescent responses to the Annexin V-FITC conjugate and the PI. The Hoechst 33342 stains the nuclei of healthy cells as well as both the apoptotic and the necrotic cells in blue fluorescence. As a result, the healthy cells can be stained only by the Hoechst 33342.

2.4.5.2. Flow cytometric analysis. To quantify the rates of apoptosis and necrosis after *in vitro* cancer hyperthermia, flow cytometry (BD FACSVerse, BD Biosciences, CA, USA) was performed by using an Annexin V-FITC Apoptosis Detection Kit. The flow cytometric analysis is based on the detection of the changes in size and granularity of cells. Unlike necrosis, apoptosis typically involves morphological changes such as cell shrinkage, DNA loss, and nuclear fragmentation. Thus, apoptotic and necrotic cells can be distinguished by the light scattering effects of the cells [44]. According to the protocol for the Annexin V-FITC Apoptosis Detection Kit, the analysis provided quantitative information on the cellular status in four quadrants: Lower left region (LL) represents viable cells (AnnexinV^-/PI^-), lower right (LR) early apoptotic cells (AnnexinV^+/PI^-), upper right (UR) late apoptotic cells (AnnexinV^+/PI^+), and upper left (UL) necrotic cells (AnnexinV^-/PI^+). In turn, the quadrant dot plots of the gated cells determined the proportion of early and late apoptotic ells. After *in vitro* MHT, the adherent cells were further incubated for 24 h. Then, the cells were harvested by using trypsin-EDTA and washed once with serum-containing cell media. After collecting 5×10^5 cells by centrifugation, the cells were re-suspended in 500 μl of 1X binding buffer. The cell suspension was incubated with 10 μg ml^{-1} of Annexin V-FITC Conjugate and PI solution for exactly 15 min at room temperature in a dark environment. For

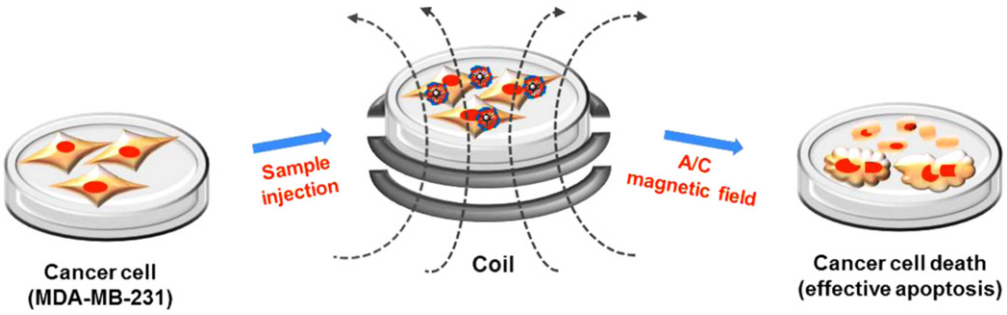

Figure 2. Schematic illustration of localized magnetic hyperthermia treatment on cancer cells.

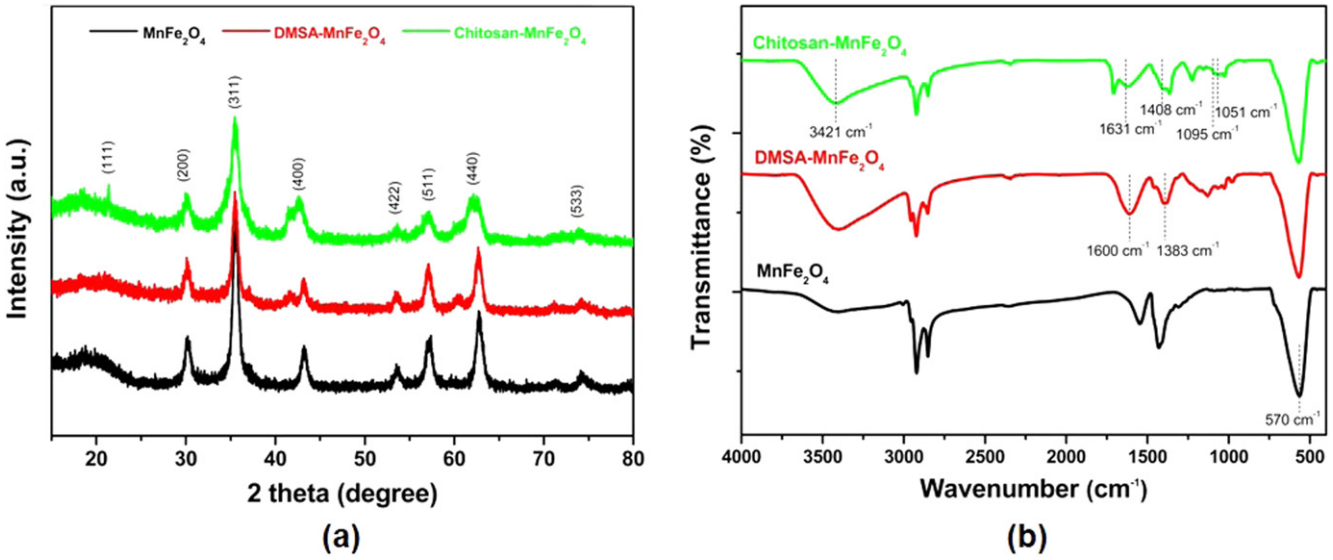

Figure 3. (a) XRD patterns and (b) FTIR spectra of $MnFe_2O_4$, DMSA-$MnFe_2O_4$, and Chitosan-$MnFe_2O_4$ nanoparticles.

double-stained compensation and quadrants, three staining tubes (untreated cells, cells stained with Annexin V-FITC, and cells stained with PI) were used as controls. The fluorescence of the cells was immediately estimated with a flow cytometer.

2.4.6. Statistical analysis. Student's t-test was used to determine any statistical significance among % apoptotic cell population data. $p < 0.05$ represents statistically significant.

3. Results

XRD was used to characterize the crystal structures of the synthesized MNPs. Figure 3(a) shows XRD patterns for the as-synthesized oleate-, DMSA-, and chitosan-coated $MnFe_2O_4$ MNPs. All the nanoparticles exhibited the distinctive peaks indexed as (111), (220), (311), (400), (422), (511), and (440), which corresponded to mixed spinel structure of $MnFe_2O_4$ (JCPDS 02-8517). No change was induced in the crystalline structure during the coating process with DMSA and chitosan.

Figure 3(b) shows FTIR spectra of $MnFe_2O_4$, DMSA-$MnFe_2O_4$, and Chitosan-$MnFe_2O_4$ nanoparticles. $MnFe_2O_4$ presented -CH_2- bands at 2922 and 2852 cm^{-1}, covalent bond between -COO^- at 1650 cm^{-1}, and an Fe-O vibration peak at 570 cm^{-1}. DMSA-$MnFe_2O_4$ demonstrated both asymmetric and symmetric stretching vibration peaks of -COO^- groups of DMSA molecules bound to $MnFe_2O_4$ at 1600 and 1383 cm^{-1}, respectively. Chitosan-coated $MnFe_2O_4$ displayed the broad band of -NH group bonded at 3430 cm^{-1}. The peak around 1631 cm^{-1} is attributed to the -NH from the primary amine and the characteristic peaks at 1408 cm^{-1} can be assigned to the symmetric vibration peak of -COO^- group. The two peaks at 1095 and 1056 cm^{-1} corresponded to the stretching vibration of C-N and C-O, respectively.

Figure 4 shows SEM/EDS analysis of the $MnFe_2O_4$ nanoparticles and table 1 shows the content of magnetic atoms for the $MnFe_2O_4$ nanoparticles determined by EDS and ICP-MS analysis. SEM/EDS was used to characterize the chemical composition of the $MnFe_2O_4$ nanoparticles [45]. The low magnification SEM image in figure 4(a) shows the surface morphology of the $MnFe_2O_4$ nanoparticles and the EDS spectrum of the $MnFe_2O_4$ nanoparticles in figure 4(b) confirms the presence of Fe, Mn, and O main element signal in the $MnFe_2O_4$ nanoparticles. The $MnFe_2O_4$ nanoparticles

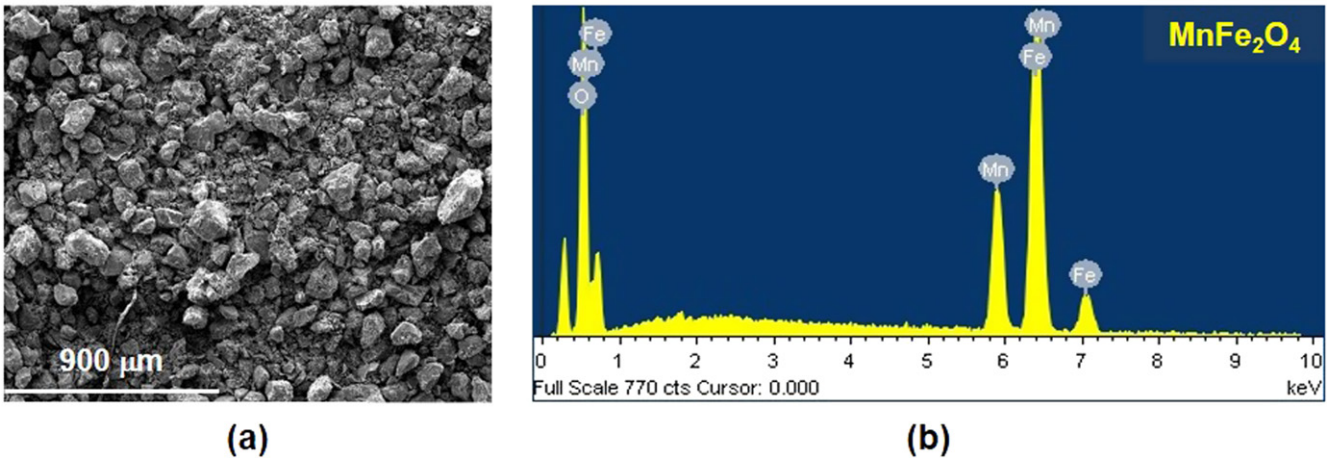

Figure 4. SEM/EDS analysis of $MnFe_2O_4$ nanoparticles.

Table 1. The elemental analysis for the $MnFe_2O_4$ nanoparticles measured by EDS and ICP-MS.

	EDS			ICP-MS		
Element	Weight (%)	Atomic (%)	Fe/Mn ratio	Weight (%)	Atomic (%)	Fe/Mn ratio
Fe	56.07	35.45	2.66	52.08	31.78	2.29
Mn	20.72	13.32	1	22.42	13.92	1
O	23.21	51.23	—	—	—	—

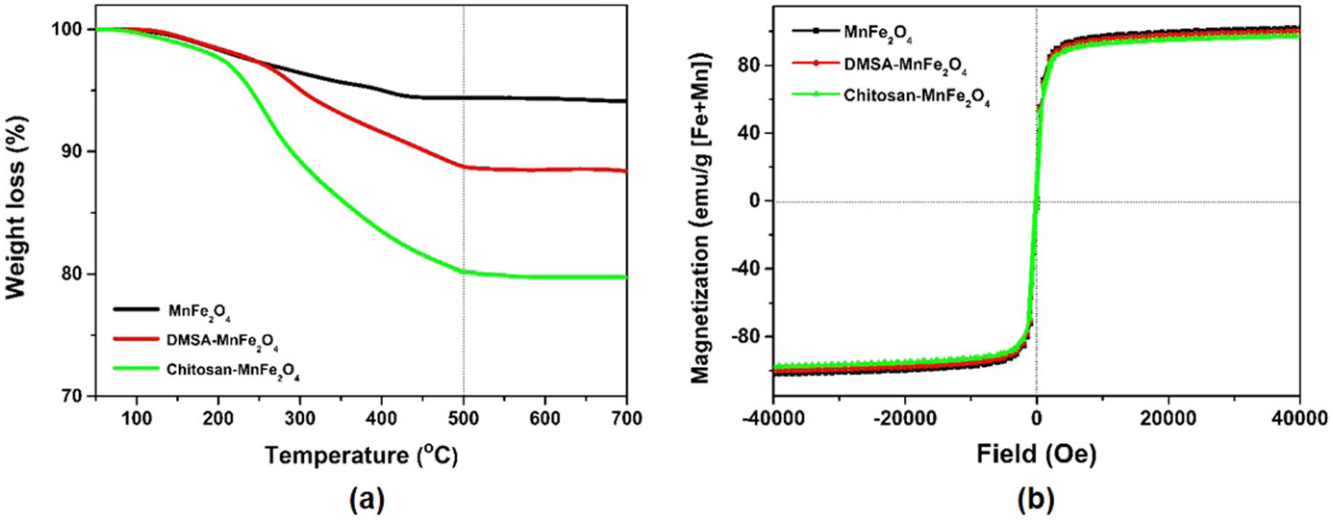

Figure 5. (a) TGA curves and (b) magnetic properties (at 300 K) of $MnFe_2O_4$, DMSA-$MnFe_2O_4$, and Chitosan-$MnFe_2O_4$ nanoparticles.

were composed of the weight fraction of Fe (56.07%) and Mn (20.72%) with the Fe/Mn atomic ratio of 2.66:1.

ICP-MS was used to analyze the mass of two magnetic elements (Fe and Mn) detected from EDS analysis on the SEM. The result from ICP-MS represented Fe (52.08%) and Mn (22.42%) of mass fraction and showed very similar elemental compositions to nanoparticles detected by EDS measurement. The average Fe/Mn atomic ratio was confirmed to be 2.29:1 by ICP-MS elemental analysis, which is close to the expected chemical formula of 2:1 (table 1).

Figure 5(a) demonstrates TGA curves of the $MnFe_2O_4$, DMSA-$MnFe_2O_4$, and Chitosan-$MnFe_2O_4$ nanoparticles to indicate the content of magnetic material on the $MnFe_2O_4$ nanoparticles. Overall, the weight of each sample gradually decreased with temperature, and the weight loss was initiated at the temperature of 120 °C, which corresponded to the removal of residual of water in the samples. In the case of the $MnFe_2O_4$ nanoparticles, due to the removal of free oleic acid and decomposition of the oleic acid molecules bound to the $MnFe_2O_4$, constant weight loss was observed with temperature. DMSA-$MnFe_2O_4$ initially showed a slight decrease in weight (around 2%) but induced a sudden weight loss at the temperature between 350 and 500 °C mainly due to decomposition of the DMSA. Compared to other nanoparticles, the

Chitosan-$MnFe_2O_4$ demonstrated relatively more considerable weight loss, resulting from the degradation of cross-linked chitosan and DMSA on the $MnFe_2O_4$ nanoparticles surface. It was noted that regardless of the nanoparticles, no significant rate of weight loss was observed at the temperatures higher than 500 °C, confirming that metal oxide existed within this temperature range [23, 25]. As a result of the temperature increase to 700 °C, the percentage change in the total weight loss (ω) of coating layer for the $MnFe_2O_4$, DMSA-$MnFe_2O_4$, and Chitosan-$MnFe_2O_4$ nanoparticles was found to be 5.60, 11.25, and 19.86%, respectively. Accordingly, the residual magnetic weight of each corresponding nanoparticle was 94.4, 88.75, and 80.14%, respectively.

Figure 5(b) presents the magnetic properties of the $MnFe_2O_4$, DMSA-$MnFe_2O_4$, and Chitosan-$MnFe_2O_4$ nanoparticles as a function of the applied field at 300 K. The magnetization curve of $MnFe_2O_4$ demonstrated zero coercivity and zero remanence, indicative of the superparamagnetic behavior of $MnFe_2O_4$. The saturation in magnetization was found at 71.45 emu g^{-1} for $MnFe_2O_4$, 66.20 emu g^{-1} for DMSA-$MnFe_2O_4$, and 58.34 emu g^{-1} for Chitosan-$MnFe_2O_4$ nanoparticles. As shown, the TGA curves (figure 5(a)), the magnetizations of both DMSA- and Chitosan-coated $MnFe_2O_4$ nanoparticles compared with those of the $MnFe_2O_4$ nanoparticles decreased because of the reduced proportion of the magnetic core comparted to the whole mass of the MNPs [46–48]. After correcting the weight fraction of the non-magnetic organic coating layer content (5.60, 11.25, and 19.86%) on the surface of the magnetic nanoparticles determined by TGA, the saturation magnetization was normalized to the mass fraction of the total magnetic atom content (74.50%) in the $MnFe_2O_4$ nanoparticles derived from ICP-MS. The final saturation magnetization value corresponding to the mass of the magnetic atoms was 101.6, 100.12, 97.71 emu g^{-1} of magnetic atoms (Fe + Mn), respectively [49, 50].

The morphology and particle size of the synthesized $MnFe_2O_4$ nanoparticles were characterized by HR-TEM and DLS measurement (figure 6) and these results were summarized as table 2. The high resolution TEM (HRTEM) images show that the MNPs are uniform cube-like monodisperse. The crystalline $MnFe_2O_4$ nanoparticles were illustrated as cubic spinel structure, and the mean size of the $MnFe_2O_4$, DMSA-$MnFe_2O_4$, and Chitosan-$MnFe_2O_4$ nanoparticles was estimated to be approximately ~18 nm (17.87 ± 1.68, 18.24 ± 1.31, and 17.63 ± 1.23 nm) according to the histogram curve fitting and showed a close-packed monodisperse $MnFe_2O_4$ nanoparticles formation with a narrow size distribution. To evaluate the hydrodynamic size and polydispersity index of the $MnFe_2O_4$, DMSA-$MnFe_2O_4$, and Chitosan-$MnFe_2O_4$ nanoparticles in dispersion, dynamic light scattering (DLS) analysis was conducted. The average hydrodynamic size of the $MnFe_2O_4$ nanoparticles in hexane was determined to be 18.36 ± 0.86 nm by DLS (figure 6(c)). And the average hydrodynamic sizes of the DMSA-$MnFe_2O_4$ and Chitosan-$MnFe_2O_4$ nanoparticles were 80.25 and 91.37 nm with a PDI of 0.27 and 0.18 in water, and 93.27 and 105.78 nm with a PDI of 0.36 and 0.29 in DMEM cell culture media, respectively. The average hydrodynamic size of the DMSA- and Chitosan-coated $MnFe_2O_4$ nanoparticles in DMEM containing proteins and salts showed about a 15% increase compared to that of water. The zeta potentials of the DMSA-$MnFe_2O_4$ and Chitosan- $MnFe_2O_4$ nanoparticles in aqueous solution were calculated to be −32.87 and +10.02 mV, respectively. The negatively-charged DMSA-coated $MnFe_2O_4$ nanoparticles can easily interact with positively-charged chitosan. So, the surface charge of the DMSA-$MnFe_2O_4$ nanoparticles coated with chitosan increased from −32.87 to +10.02 mV. Because of the surface charge and steric stabilization, the DMSA- and Chitosan-coated $MnFe_2O_4$ nanoparticles showed excellent stability in aqueous suspension, even at DMEM cell culture media containing high salt concentration (inset figure 6).

Figure 7 exhibits the cell viability of the DMSA-$MnFe_2O_4$ and Chitosan-$MnFe_2O_4$ nanoparticles at various concentrations (i.e. 0.1, 0.5, 1.0 and 1.5 mg magnetic atoms/ml) after 24, 48, and 72 h incubation. The control represented MDA-MD-231 cells without MNPs and presented no change in the cell viability for all the incubation times. In the case of the DMSA-$MnFe_2O_4$ nanoparticles, the cell viability decreased with both concentration and incubation time. At the highest concentration (1.5 mg magnetic atoms/ml) and longest incubation time (72 h), DMSA-$MnFe_2O_4$ presented almost 20% lower cell viability, in comparison with the control. On the other hand, regardless of concentrations, the Chitosan-$MnFe_2O_4$ nanoparticles presented almost comparable cell viability at each incubation time but sustained slightly lower viability than the control. At 1.5 mg magnetic atoms/ml and 72 h incubation time, the Chitosan-$MnFe_2O_4$ nanoparticles still yielded 91.49% cell viability without significant cytotoxic effect. The increased cell viability of the Chitosan-$MnFe_2O_4$ nanoparticles even at the high concentrations resulted from the non-toxic and biocompatible properties of chitosan. In turn, the surface-modified $MnFe_2O_4$ nanoparticles coated by a bilayer of DMSA and chitosan provided, were an excellent biocompatible product and can be used in many biologically relevant applications.

Figure 8 and table 3 show cellular uptake affinity using the Chitosan-$MnFe_2O_4$ nanoparticles onto an MDA-MB-231 breast cancer cell as an indicator cellular uptake. Figure 8 shows intracellular uptake of the Chitosan-$MnFe_2O_4$ nanoparticles for the MDA-MB-231 cell visualized using Prussian blue staining. After Prussian blue staining, most of cells were stained with blue stains inside the cells, indicating cell uptake of the Chitosan-$MnFe_2O_4$ nanoparticles. As the incubation time increases, the labeled cells by Prussian blue staining were gradually accumulated into the cells in accordance with the cell population as incubation time increases. As a result of the cell morphology with Prussian blue staining, 1.5 mg magnetic atoms/ml of the Chitosan-$MnFe_2O_4$ nanoparticles at 72 h of incubation displayed an excellent cellular uptake rate into the cells and was non-toxic for the MDA-MB-231 cells. Table 3 represents quantitative cell uptake analysis measured by ICP-MS after 24, 48, and 72 h incubation. Cells with 1.5 mg magnetic atoms/ml of the Chitosan-$MnFe_2O_4$ nanoparticles were accumulated 97.92 (±2.55%), 111.72

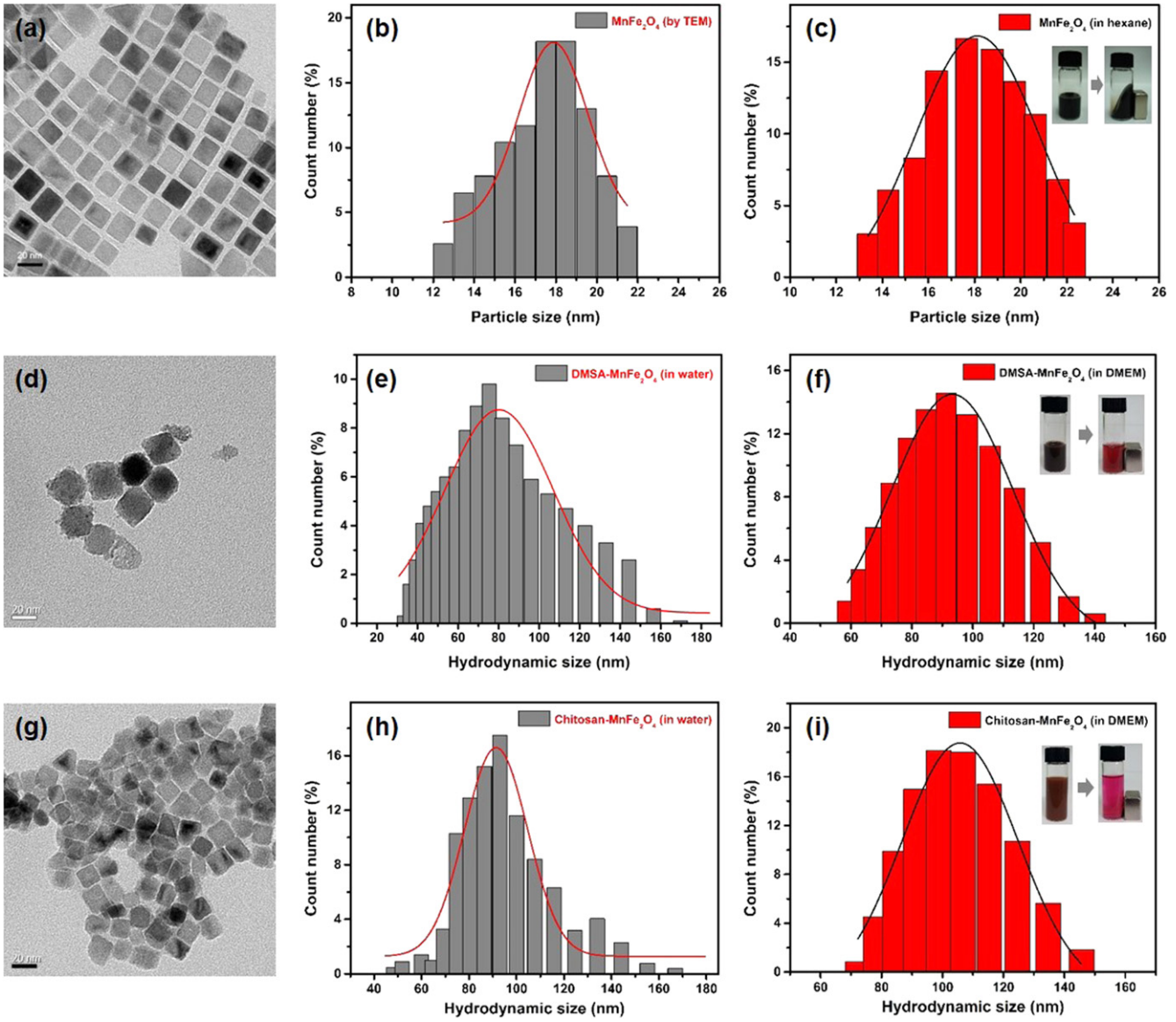

Figure 6. TEM images of 18 nm sized $MnFe_2O_4$, DMSA-$MnFe_2O_4$, and Chitosan-$MnFe_2O_4$ nanoparticles (100 000×; bar = 20 nm) (a), (d), (g). Particle distributions of $MnFe_2O_4$ nanoparticles estimated by TEM (b) and DLS (c) in hexane, and hydrodynamic size of DMSA-$MnFe_2O_4$ and Chitosan-$MnFe_2O_4$ nanoparticles measured by DLS in water (e), (h) and DMEM cell culture medium (f), (i). Inset: photographs of the dispersion and magnetic separation of $MnFe_2O_4$ nanoparticles in hexane, and DMSA-$MnFe_2O_4$ and Chitosan-$MnFe_2O_4$ nanoparticles in DMEM cell medium).

Table 2. Particle diameter (PS), hydrodynamic (HD) size, PDI, and zeta potential of functionalized $MnFe_2O_4$ nanoparticles.

		PD (nm) (by TEM)	HD size (nm) (by DLS)	PDI	HD size (nm)	PDI	Zeta potential (mV)
Sample name	Modification	—	Water	Water	DMEM	DMEM	Water
$MnFe_2O_4$	- Oleic acid	17.87 (±1.68)	18.36 (±0.86) (in hexane)	—	—	—	—
DMSA-$MnFe_2O_4$	- DMSA	18.24 (±1.31)	80.25 (±26.73)	0.27	93.27 (±19.98)	0.36	−32.87
Chitosan-$MnFe_2O_4$	- Chitosan	17.63 (±1.23)	91.37 (±13.33)	0.18	105.78 (±19.05)	0.29	+10.02

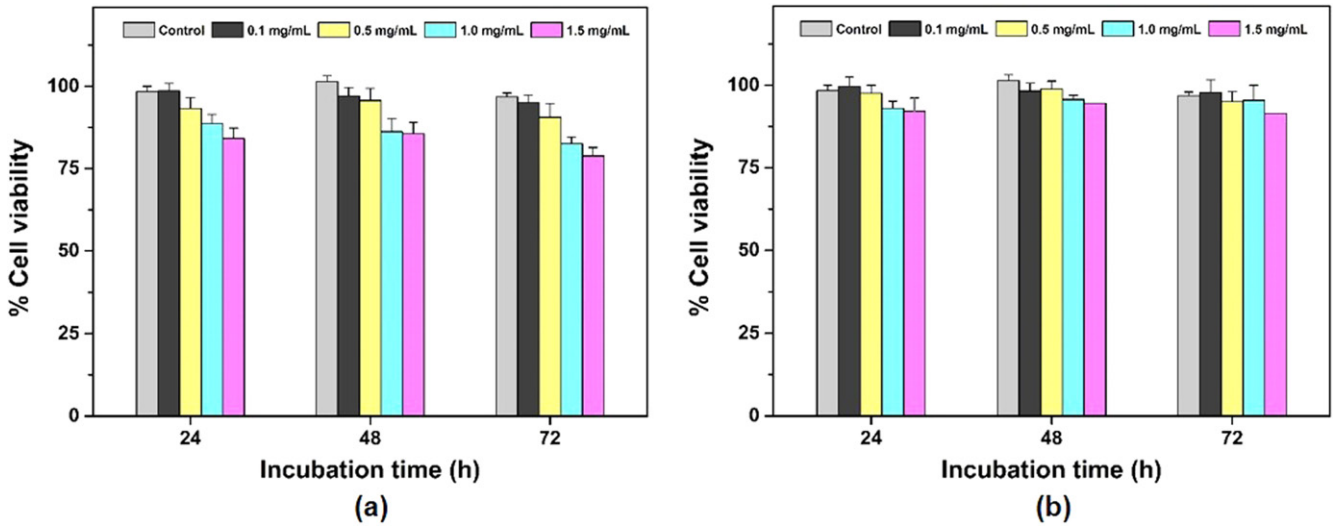

Figure 7. Cell viability of (a) DMSA-$MnFe_2O_4$ and (b) Chitosan-$MnFe_2O_4$ nanoparticles at various concentrations (0.1, 0.5, 1.0, and 1.5 mg magnetic atoms/ml) and incubation times (24, 48, and 72 h). Each error bar is one standard deviation.

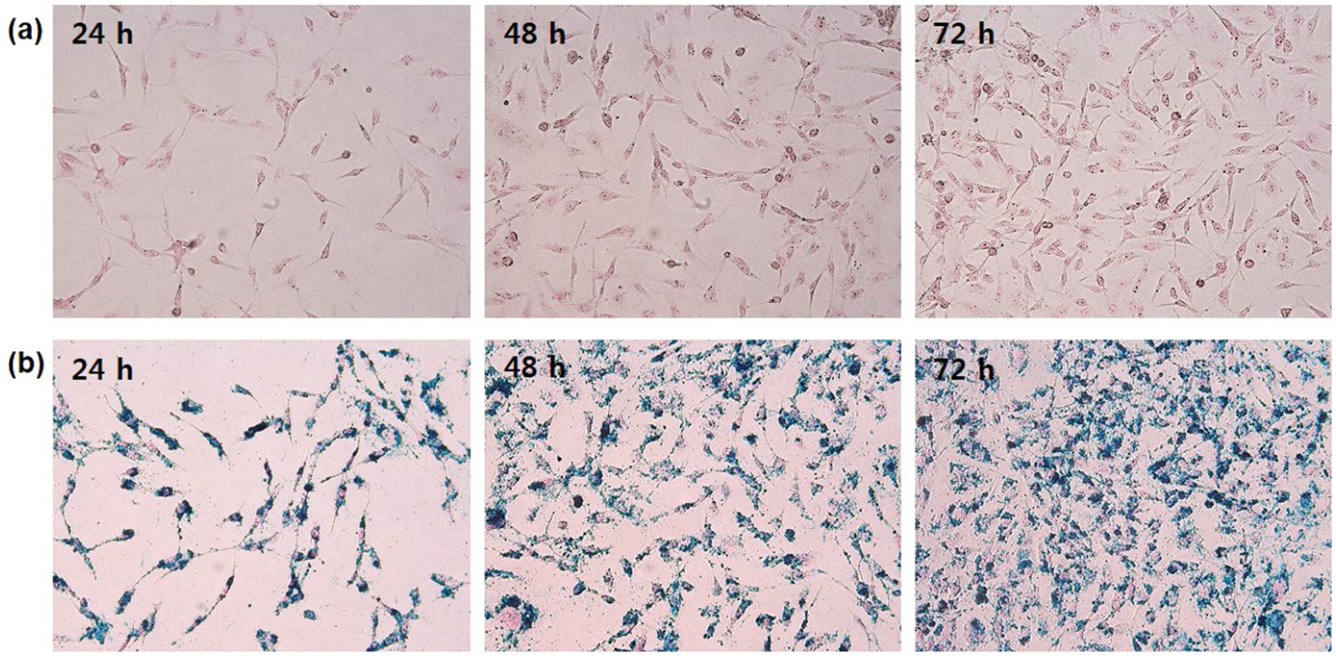

Figure 8. Cellular uptake of Chitosan-$MnFe_2O_4$ nanoparticles (a) control, and (b) 1.5 mg magnetic atom/ml by Prussian blue staining.

Table 3. Calculated cellular uptake rate of magnetic atoms (Mn+Fe) by ICP-MS.

Incubation time	24 h	48 h	72 h
Uptake (*pg* magnetic atom/cell)	97.92 (±2.55%)	111.72 (±1.25%)	145.74 (±3.15%)

(±1.25%), and 145.74 (±3.15%) *pg* magnetic atoms/cell at different incubation times (24, 48, and 72 h), respectively. As incubation time increased, cell uptake rate was also increased. In addition, the Chitosan-$MnFe_2O_4$ nanoparticles were demonstrated to exhibit high magnetic atom uptake efficiency for the MDA-MB-231 cancer cell.

Figure 9 shows the temporal development of temperature and SAR with the corresponding maximum temperature in aqueous solution of the Chitosan-$MnFe_2O_4$ nanoparticles (1.5 mg magnetic atoms/ml) at various AC magnetic field amplitudes from 20 to 60 kA m^{-1}. Overall, temperature increased with the magnetic field amplitude and heating time. At the higher magnetic field amplitudes, the temperature became saturated. Both SAR and the maximum temperature presented a linear relationship with the magnetic field amplitude. The measured SAR was 57.2, 97.5, 152.21, 209.41, and

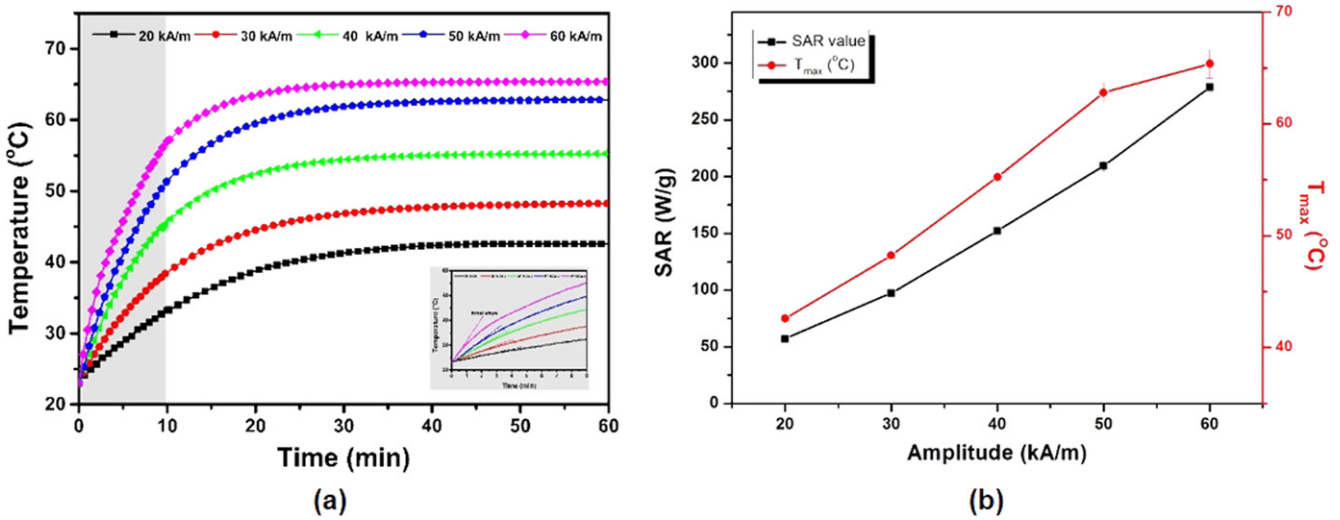

Figure 9. Characterization of Chitosan-$MnFe_2O_4$ nanoparticles in 1 ml of aqueous solution (1.5 mg magnetic atoms/ml) at various AC magnetic field amplitudes from 20 to 60 kA m^{-1} (at 307 kHz): (a) temporal development of temperature and maximal initial slope (inset), and (b) SAR with the corresponding maximum temperature.

278.69 W g^{-1}, which corresponded to the maximum temperatures of 44.10, 48.24, 55.25, 62.81, and 65.38 °C, respectively. As a result of thermal response curves, SAR values and the maximum temperature rise also increased with increasing applied AC magnetic field strength.

Figures 10(a) and (b) quantitatively compare the degree of hyperthermal efficiency and SAR (W/g) for Feridex and the Chitosan-$MnFe_2O_4$ nanoparticles at the same concentration of 1.5 mg magnetic atoms/ml. Both the control and Feridex showed comparable temperature development linearly with bearing time (figure 10(a)). Compared to Feridex, the Chitosan-$MnFe_2O_4$ nanoparticles entailed a roughly 11-fold rapid temperature increase, and after 10-min heating, Feridex and the Chitosan-$MnFe_2O_4$ nanoparticles reached 26.15 and 51.36 °C, respectively. In order to evaluate the degree of hyperthermal efficiency, SAR (W/g) of each sample was quantitatively compared in figure 10(a). Apparently, the SAR value of the Chitosan-$MnFe_2O_4$ nanoparticles (209.41 W g^{-1}) was more than nine times as high as that of Feridex (22.35 W g^{-1}). Figure 10(b) shows the *in vitro* hyperthermic effect of the Chitosan-$MnFe_2O_4$-applied MHT on the MDA-MB231 cells. For localized heating, three AC magnetic fields (25, 35, and 50 kA m^{-1}) were applied for 30 min to the cells with 1.5 mg magnetic atoms/ml of MNPs and compared in terms of temperature. In the case of the 50 kA m^{-1} application, the temperature continued to increase at the rate of 4.4 °C/min and gradually became saturated around 70 °C. To achieve and sustain the therapeutic temperatures of 42 and 52 °C, the magnetic field was initially applied at 50 kA m^{-1} and then reduced to 20 and 35 kA m^{-1}. Both the therapeutic temperatures acquired 2.5 and 5 min respectively after the initiation of MHT, and the temperatures were constantly maintained (±0.5 °C) (figure 10(c)). Figure 10(d) shows the temperature gradient of the MDA-MB-231 cells in a 35 mm cell culture dish measured by an IR thermal camera (FLIR systems, i5, Oregon, USA). The IR thermal camera image displayed a little inhomogeneous temperature distribution in the cell culture dish due to inhomogeneous dissipation of heat from the sample into its surrounding environment under non-adiabatic conditions [51, 52]. The difference between the high (41.8 °C) and low temperature (40.4 °C) in the cell dish during cancer hyperthermia was 1.4 °C. Variations in temperature within the range of hyperthermia therapeutic temperature (42 ~ 45 °C) do not affect the efficiency of MHT during cancer hyperthermia.

Figure 11 displays cytotoxic effects of the Chitosan-$MnFe_2O_4$-applied MHT on the MDA-MB231 cells at various treated conditions and incubation times (0, 24, and 48 h). Both the control and CM showed no marked change in the cellular apoptotic activity for all the incubation times (figures 11(a) and (b)), which were saturated with densely packed organization of the cell layers. In figure 11(c), HT-42 partially displayed condensed morphology but hardly presented DNA breakage and decrease in cell population. Thus, the cells with neither magnetic particles nor magnetic fields sustained insignificant cytotoxic effects for all the incubation times. However, MHT-42 demonstrated that after 24 h incubation, nuclear membrane in the cells was damaged in the form of nuclear collapse and membrane blebbing. After 48 h incubation, the nucleus began to break apart and the DNA broke into small pieces. In addition, post-MHT-42 yielded cell fragmentation and the formation of several apoptotic bodies in most of the cells. Along with severe morphological changes in the cell bodies, the cells underwent significant disruptions in figure 11(d). Lastly, for MHT-52, the cells started to condense into a large agglomerate instantly after 24 h incubation (figure 11(e)). As the incubation time increased, the dead cells suspended in the cell dish increased without apoptotic fragments. After 48 h incubation, almost 100% cellular death was observed in figure 11(e).

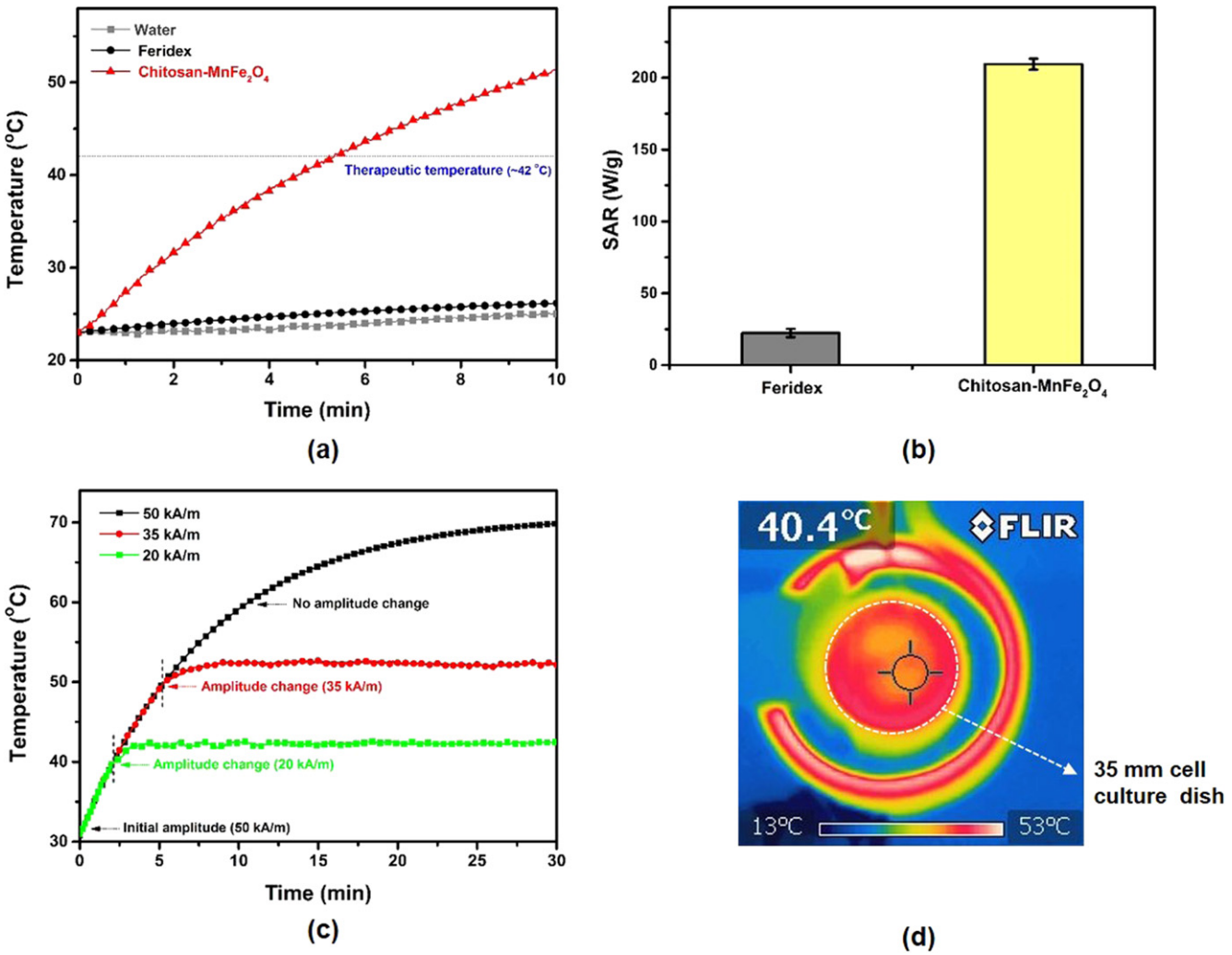

Figure 10. Comparison of thermal responses between Feridex and Chitosan-$MnFe_2O_4$ nanoparticles in 1 ml of aqueous dispersion (1.5 mg magnetic atoms/ml) under an AC magnetic field (at 307 kHz and 50 A m^{-1}): (a) temperature variations and (b) SAR. Water was used as the control. (c) Thermal responses, and (d) temperature gradient of MDA-MB231 cells during *in vitro* cancer hyperthermia with 1.5 mg magnetic atoms/ml of Chitosan-$MnFe_2O_4$ nanoparticles in a 35 mm cell culture dish of 1 ml of cell medium at various AC magnetic field amplitudes (20, 35, and 50 kA m^{-1}).

Figure 12 demonstrates fluorescence microscopic images of the MDA-MB-231 cells with 1.5 mg magnetic atoms/ml of Chitosan-$MnFe_2O_4$ nanoparticles after 24 h incubation to evaluate the efficiency of MTH. A Hoechst 33342 assay and Annexin V-FITC Apoptosis Detection Kit were used to qualitatively distinguish the progression of apoptosis and necrosis under various testing conditions. The control and CM showed no green and red fluorescence induced by Annexin V-FITC and PI double staining in figures 11(a) and (b), indicating no apoptotic and necrotic cell death. Blue fluorescence from the Hoechst 33342 and overlay images also represented approximately 100% live cells, which mirrors no effect of MNPs on the cellular death (i.e., no green or red fluorescence). On the other hand, HT-42 presented a low degree of early apoptosis (green fluorescence from Annexin V FITC) and late apoptosis/necrosis (red fluorescence from PI) in figure 12(c). Once the cells were magnetically treated with MNPs at 42 °C (MHT-42), both intense green and red fluorescence lights were considerably generated in figure 12(d). Due to the intensity of green and red fluorescence, MHT-42 was a more efficient cancer treatment than HT-42 in light of early apoptosis (green) and late apoptosis/necrosis (red). As the overlay image for MHT-42 confirmed that all the fluorescence lights (blue, green, and red) were almost overlapped at the same position, the number of viable cells quickly decreased and the apoptosis proceeded from the early to the late stage within 24 h after MHT at 42 °C. In the case of MHT-52, relatively stronger red fluorescence from PI was observed than green fluorescence. According to the overlay images, MHT-52 apparently yielded more necrotic cells than MHT-42.

Figure 13 shows flow cytometric analysis on apoptosis and necrosis of the MDA-MB-231 cells at various testing conditions with or without the Chitosan-$MnFe_2O_4$ nanoparticles and AC magnetic field after 24 h incubation. Cellular death due to apoptosis and necrosis was examined with Annexin V-FITC and PI double staining after cancer treatment. The morphological changes in the dying cells were

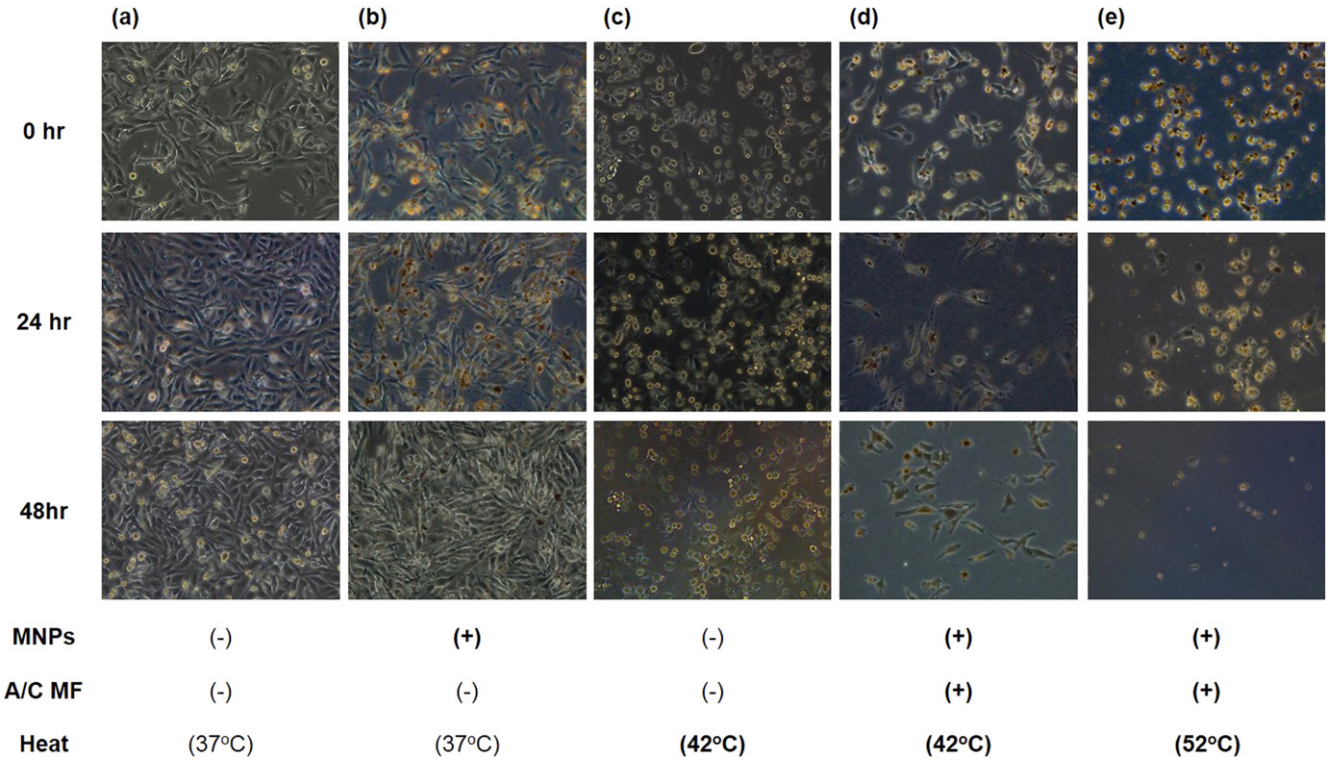

Figure 11. Microscopic images of MDA-MB-231 cells with 1.5 mg magnetic atoms/ml of Chitosan-$MnFe_2O_4$ nanoparticles at different incubation times (0, 24, and 48 h): (a) the control (untreated cells without MNPs and MF), (b) CM (cells treated with MNPs and without MHT), (c) HT-42 (cells treated without MNPs and MHT and incubated at 42 °C), (d) MHT-42 (cells treated with MNPs and MHT at 42 °C), and (e) MHT-52 (cells treated with MNPs and MHT at 52 °C).

distinguished by the dot-plot patterns of the cell distribution, and the percentages of cell populations in each quadrant were compared. In figures 13(a) and (b), both the control and CM presented a comparable distribution of the viable cells in LL (i.e., 93.2 and 90.2%, respectively). Compared to the control cells, CM showed a slight decrease in the viable cell populations. According to figure 13(c), the MDA-MB-231 cell populations were marginally shifted from LL to LR, UL, and UR, in comparison with the control, representing the initiation of early- and late-apoptosis in the cells. However, for MHT-42 in figure 13(d), a substantial increase in the cell populations was found in LR (42.2%) and UR (32.9%), evidencing the incidence of significant apoptosis in the cells. For MHT-52 in figure 13(e), the cell populations increased exclusively in UL (77.0%), indicating that necrosis became dominant, compared to MHT-42. Figure 13(f) represents a comparison of the quantitative analysis on viable, total apoptosis, and necrosis in cell population at different cancer treatment conditions. Both the control and CM demonstrated that most cells were viable (i.e., 93.2% for control and 92.5% for CM). HT-42 showed a slight decrease in the viable cell populations (72.7%) but a slight increase in both the total apoptosis and the necrosis populations (21.4 and 5.9%, respectively). On the other hand, MHT-42 exhibited a significant decrease in the viable cell populations (22.6%) but a considerable increase in the total apoptosis cell populations (75.1%) after MHT with MNPs. Both HT-42 and MHT-42 indicated that the cellular death was induced mainly by apoptosis after hyperthermia at 42 °C with or without the Chitosan-MnF_2O_4 nanoparticles and AC magnetic field. For MHT-52, the cell populations for viable, total apoptosis, and necrosis were 17.9, 5.2, and 76.7%, respectively. In contrast to HT-42 and MHT-42, MHT-52 confirmed that necrosis was primarily responsible for the cellular death as apoptotic cells were rarely detected, which well agreed with the observations from the optical and fluorescence imaging in figure 12.

4. Discussion

4.1. Properties and biocompatibility of Chitosan-$MnFe_2O_4$ nanoparticles

Monodisperse $MnFe_2O_4$ nanoparticles were prepared by a high-temperature decomposition reaction of metal acetylacetonate. For hyperthermia experiments, MNPs should have high SAR values in order to accomplish therapeutic temperatures (42 ~ 45 °C) with minimal particle concentrations [53]. The SAR value is highly dependent on the properties of MNPs such as composition doped-metal, mean size, and shape. In the recent study on spinel metal ferrites, the specific magnetization of Mn-doped iron oxide nanoparticles ($MnFe_2O_4$) were shown to have a relatively high mass magnetization increase due to the increase in the magnetic moment and crystalline by Mn substitution. Mn-ferrite nanoparticles display low inherent toxicity and high thermal energy transfer capability [54]. Thus, they are considered as

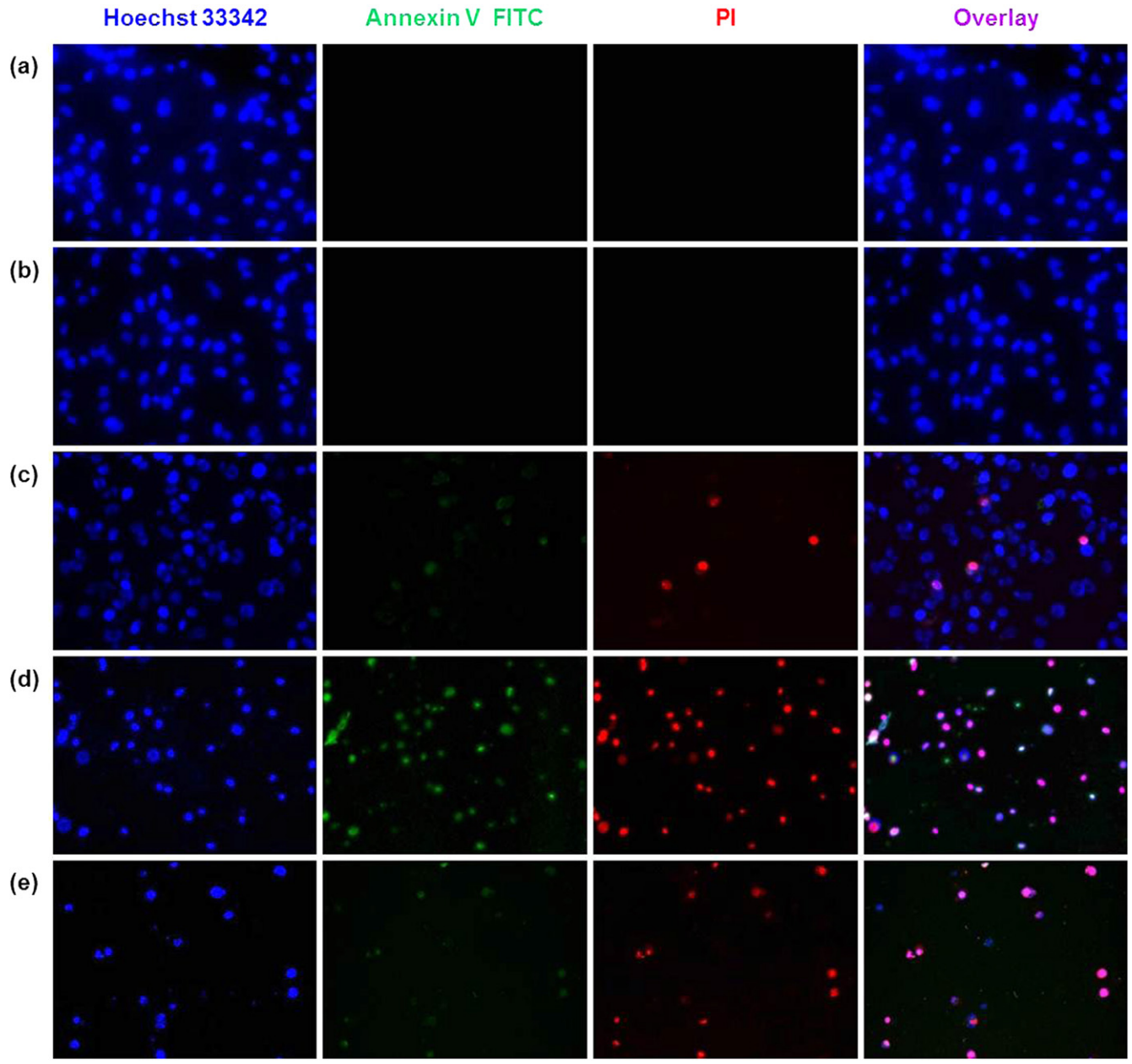

Figure 12. Fluorescence microscopic images of MDA-MB-231 cells with 1.5 mg magnetic atoms/ml of Chitosan-$MnFe_2O_4$ nanoparticles after 24 h incubation: (a) the control (untreated cells without MNPs and MHT), (b) CM (cells treated with MNPs and without MHT), (c) HT-42 (cells treated without MNPs and MHT and incubated at 42 °C), (d) MHT-42 (cells treated with MNPs and MHT at 42 °C), and (e) MHT-52 (cells treated with MNPs and MHT at 52 °C). The cells were stained with Hoechst 33342 and Annexin V FITC/PI conjugate staining agents.

efficient magnetic hyperthermia agents. Recently, synthesis of Mn ferrite nanoparticles for *in vitro* hyperthermia applications were reported by Markridis *et al* [31, 55, 56]. In this study, Mn-ferrite nanoparticles showed high SAR value (455.3 W g^{-1}) under an AC magnetic field at high frequency (765 kHz). The SAR value is proportional to the frequency and magnetic field strength but it is not normalized against the frequency and magnetic field strength. Because the SAR value can vary the different experimental setups, it is difficult to compare the heating efficiency of magnetic nanoparticles by SAR calculation. For effective cancer hyperthermia, the intrinsic heating efficiency of magnetic nanoparticles should be improved. The heating efficiency is dependent on the properties of magnetic nanoparticles such as magnetization, anisotropy, size, and hydrodynamic size distribution.

The magnetic property is strongly related to the size of the nanoparticles. In most of the studies, MNPs in very small size (<5 nm) have a disordered spin layer at their surfaces, and the surface spin disorder of the small nanoparticles can cause a reduction in magnetization. The heat generation of MNPs is also proportional to the size of MNPs smaller than 20 nm due to Néel–Brownian relaxations and the mechanism of heat loss [57–60]. Thus, the optimal particle size becomes a critical tuning parameter for MHT [61, 62]. Furthermore, the

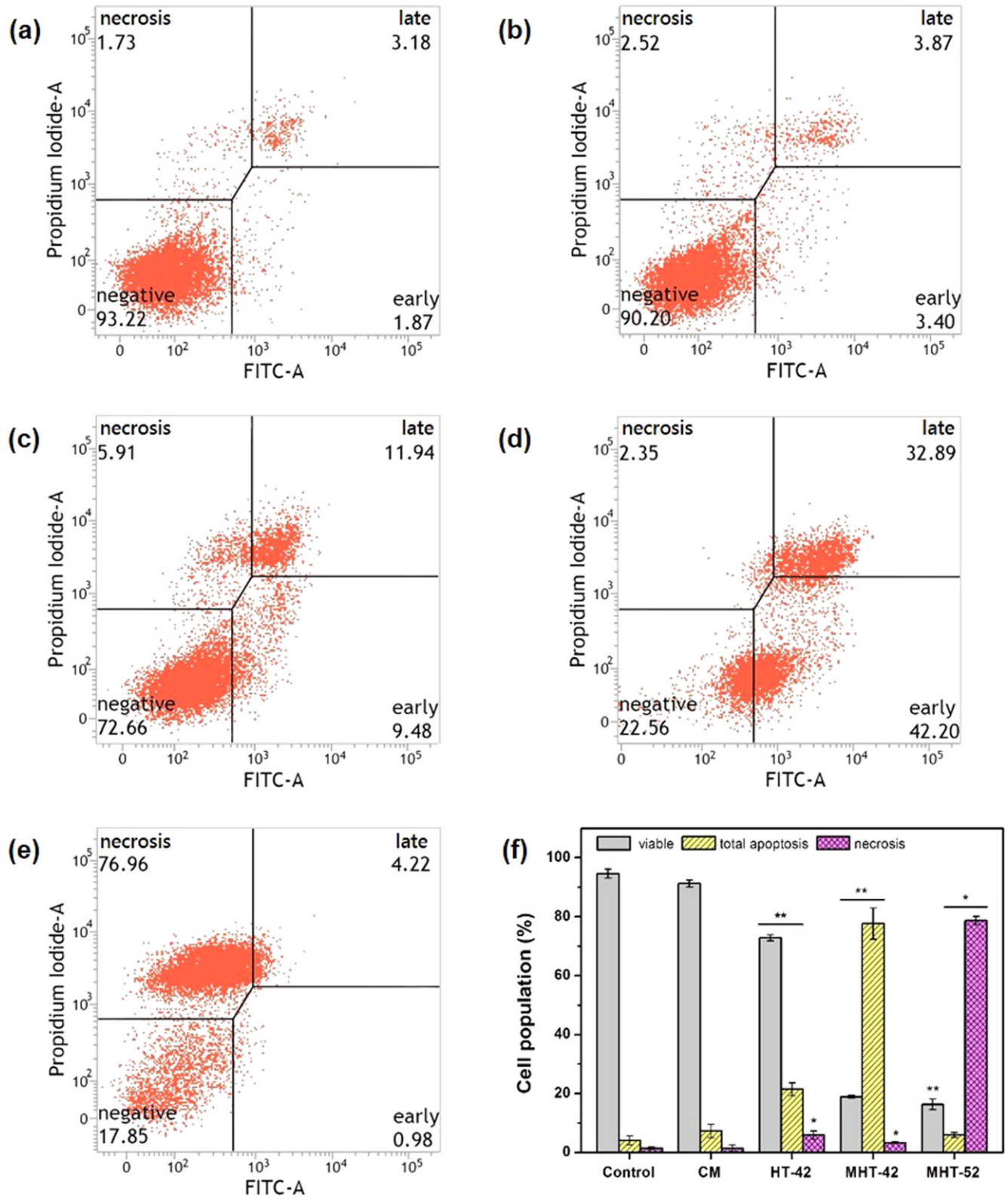

Figure 13. Flow cytometry analysis on apoptosis and necrosis of MDA-MB-231 cells using Annexin V-FITC Apoptosis Detection Kit I assay at different conditions: (a) the control (untreated cells without MNPs and MHT), (b) CM (cells treated with MNPs and without MHT), (c) HT-42 (cells treated without MNPs and MHT and incubated at 42 °C), (d) MHT-42 (cells treated with MNPs and MHT at 42 °C), (e) MHT-52 (cells treated with MNPs and MHT at 52 °C), and (f) quantitative analysis of percentage of gated cells for viable, necrotic, total (early and late) apoptosis. * and ** mean $p < 0.05$ and $p < 0.005$ (significant) respectively. MNPs concentration = 1.5 mg magnetic atoms/ml and incubation time = 24 h.

SAR value is related to the shape of the nanoparticles. In particular, cubic-shaped nanoparticles can form flat faces and contain fewer defects in their structures. Due to the regular surface definition, the cubic-shaped nanoparticles have a higher magnetization, compared with that of spherical-shaped nanoparticles associated with defected surface structures. In fact, the cubic-shaped nanoparticles with densely packed systems have shown that dipolar interactions affect not only susceptibility, but the blocking temperature transition as well as particle motion in solution [63]. Therefore, the cubic-shaped nanoparticles can provide high heat generation due to higher magnetization and more well-packed crystalline shape than that of the spherical-shaped nanoparticles [20, 63, 64]. As the current superparamagnetic $MnFe_2O_4$ nanoparticles represented uniform cubic shape with a size of 18 nm, the $MnFe_2O_4$ nanoparticles with high magnetization can be an effective agent for MHT.

For biomedical applications, as-synthesized hydrophobic MNPs were modified with hydrophilic ligands. In this study, chitosan was chosen owing to its excellent biocompatibility and high hydrophilicity. In addition, a number of hydroxyl and amino groups of chitosan facilitates further modifications with various organic molecules. However, incomplete coating of chitosan could cause the loss of colloidal stability in aqueous solution. Because it is difficult to conjugate chitosan directly onto the hydrophobic nanoparticles, the $MnFe_2O_4$ nanoparticles were modified with DSMA by ligand exchange prior to chitosan coating. The DMSA-coated $MnFe_2O_4$ nanoparticles exhibited excellent colloidal stability in aqueous solution due to the formation of a stable coating through carboxylate chelate bonding and intermolecular disulfide cross-linking between ligands. In addition, the negatively-charged DMSA encapsulating the surface of MNPs readily facilitated the binding of positively-charged chitosan via electrostatic interactions. Moreover, the presence of a large number of primary amine groups in a chitosan-coating layer on the $MnFe_2O_4$ core was able to increase the stability in a buffer solution without aggregation and to increase the affinity between the nanoparticles and the negatively-charged cell surface. It is thus conceivable that well-dispersed MNPs in aqueous media could provide a uniform distribution of heat source, contributing to the delivery of homogeneous heating to the target area and avoiding any localized hot spot. In the current study, chitosan was coated onto the surface of the DMSA-$MnFe_2O_4$ nanoparticles using an EDC cross-linking agent that could control the coating thickness. It was reported that the synthesis of chitosan-coated MNPs using an ionic gelation or glutaraldehyde cross-linking agent usually yielded micron-sized chitosan nanoparticle complexes [32, 65]. Thus, EDC enabled the Chitosan-$MnFe_2O_4$ nanoparticles to obtain higher magnetization values, which could virtually be effective for hyperthermia applications.

4.2. Characteristic features of Chitosan-$MnFe_2O_4$ nanoparticles

Both XRD peaks and line broadening in XRD pattern verified the crystalline structure and size of $MnFe_2O_4$ in figure 3(a). Since the ionic radii of both Mn^{2+} and Fe^{2+} ions were of equivalent size, the substitution of Fe^{2+} by Mn^{2+} was feasible, and thus, Mn^{2+} substitution did not induce a significant change in particle size. In addition, TEM images in figure 6(a) confirmed that the mean size of $MnFe_2O_4$ was 17.87 ± 1.68 nm. Theoretically, the mean size of the $MnFe_2O_4$ crystalline nanoparticles, D, can be determined by the Debye–Scherrer equation as follows [66]:

$$D = \frac{K\lambda}{\beta \cdot \cos\theta}$$

where K is a constant related to crystallite shape (i.e. $K = 0.94$ for Cu-K), λ the x-ray wavelength in nanometer (i.e. $\lambda = 0.154$ nm for Cu-K), β the peak width of the diffraction peak profile at half maximum height, and θ the diffraction angle. The mean size of the $MnFe_2O_4$ nanoparticles could be estimated to be 18 nm, comparable to the size measured in TEM (figure 6). Thus, the surface modification with coating materials hardly varied the structure and morphology of the fabricated $MnFe_2O_4$.

After ligand exchange with DMSA, the two peaks of carboxylic acid-iron bonds of DMSA-$MnFe_2O_4$ were significantly shifted to 1600 and 1383 cm^{-1} (figure 3(a)). The appearance of peaks at 1600 and 1380 cm^{-1} suggested that the DMSA coated to the surface of the $MnFe_2O_4$ nanoparticles in place of oleic acid. In addition, the C=O stretching vibration of the formed amide at 1631 cm^{-1} confirmed the coating of chitosan to $MnFe_2O_4$. Hence, both DMSA and chitosan were successfully bound to the surface of the $MnFe_2O_4$ nanoparticles.

TGA thermograph measured the fraction of the organic material on the MNPs. The TGA curve for the $MnFe_2O_4$ nanoparticles showed that weight loss continued over the entire temperature from 30 to 700 °C. The weight loss at low temperature could be associated with boiling and decomposition of residual water and free organic material in the sample, whereas the loss at high temperature represented strong binding between the coating organic materials and $MnFe_2O_4$ nanoparticles.

The residual hysteresis loop in figure 5(b) confirmed superparamagnetic behavior of Chitosan-$MnFe_2O_4$. It is conceived that no or minimal magnetic attraction-induced agglomeration could be anticipated during *in vivo* transportation of MNPs to in the intravascular system under an AC magnetic field. Apparently, the magnetization value of the $MnFe_2O_4$ nanoparticles decreased as the coating thickness increased and the diminished magnetic feature was attributed to the thickness of inactive coating shell layers, leading to a reduction in the effective weight fraction of the magnetic core in the nanoparticles.

4.3. Colloidal stability in biological media

When the magnetic nanoparticles were used in biological media for *in vitro* and *in vivo* cell study, most of the nanoparticles first interact with the biomolecules and salts in the cell culture medium, and then their surface properties change greatly because of the nanoparticles-proteins aggregates [67–

69]. The adsorption of proteins on the magnetic nanoparticles leads to the gradual increase in particle size and the aggregation. For *in vitro* and *in vivo* biomedical applications, it is crucial to obtain colloidal stability of the dispersion in biological media to avoid the formation of aggregates. The surface charge determined by zeta potential measurement is an important parameter for the colloidal stability in dispersion media. Highly negatively-charged DMSA-$MnFe_2O_4$ nanoparticles with zeta potential of −33 mV have an excellent colloidal stability by the electrostatic repulsive force. But, when DMSA-$MnFe_2O_4$ nanoparticles are dispersed in cell medium, their zeta potential is increased due to the effect of surface charge neutralization by Na^+ binding [70]. These results imply that the colloidal stability of the DMSA-$MnFe_2O_4$ nanoparticles is reduced with the increase of NaCl concentration and may lead to an increase in hydrodynamic size in the cell culture media [71]. Generally, nanoparticles with a low zeta potential show a poor stability in cell culture media. However, the chitosan-coated $MnFe_2O_4$ nanoparticles with a low zeta potential of +10.02 mV show a good the colloidal stability because of the specific features of the chitosan such as its hydrophilic nature, which provides more intense repulsive hydration forces, and steric stabilization, which prevents the protein adsorption by the brush-type conformation of adsorbed chitosan chains [72].

4.4. NP internalization

Although chitosan-coated $MnFe_2O_4$ nanoparticles are non-specific for the MDA-MB-231 breast cancer cell, they showed high cell uptake affinity (figure 10 and table 2). This was attributed to the unique properties of chitosan. First, due to its mucoadhesive properties, chitosan has an absorption enhancing effect through epithelial tight junction openings [54]. Moreover, chitosan surface-modified nanoparticles enhanced cellular uptake by adsorptive endocytosis compared to that of chitosan solution. But, the uptake efficiency of chitosan was affected by chitosan molecular weight and diameter [73]. Chitosan has a high molecular weight (20 ∼ 200 kDa). In addition, after being dispersed in the culture medium including protein, the hydrodynamic diameter was greatly increased [74]. Because endocytosis is size dependent, the bigger size of aggregated nanoparticles may interfere with cellular uptake. Chitosan, having abundant positive NH^{2+} groups, is more effective to bind medium protein and also to cross-link other negatively-charged molecules. To overcome this agglomeration, in this study, positively-charged chitosan (+51.0 mV) was combined onto the surface of highly negatively-charged DMSA-$MnFe_2O_4$ (−32.87 mV) *via* electrostatic interaction. The difference in the zeta potential between chitosan and the DMSA-$MnFe_2O_4$ nanoparticles involves the neutralization of the carboxyl group and ammonium ions due to the electrostatic interaction. Thus, the zeta potential of the chitosan-coated $MnFe_2O_4$ nanoparticles was around +10.02 mV [65, 74]. The PDI of the as-synthesized Chitosan-$MnFe_2O_4$ nanoparticles was 0.18. Generally, PDI values, greater than 0.7, indicate that the sample has a broad size distribution including irregular different size and aggregation. In contrast, because Chitosan-$MnFe_2O_4$ nanoparticles (PDI = 0.18) have monodisperse particles and narrow particle distribution, they can pass the cell barrier. Eventually, due to the zeta potential and low PDI value, Chitosan-$MnFe_2O_4$ nanoparticles display excellent stability in water and cell medium without any aggregation.

4.5. SAR values and hyperthermic effect

Chitosan-$MnFe_2O_4$ nanoparticles under magnetic field convert the applied magnetic field into thermal energy, resulting in temperature increase. Heat dissipation from relaxation loss depends on the viscosity of the surrounding environment and properties of magnetic nanoparticles such as magnetic core and hydrodynamic size of magnetic nanoparticles, the saturation magnetization, and anisotropy of magnetic nanoparticles. A lot of heat induced by magnetic hypertherthermia transfers the water-based cell medium surrounding the cells. Thus, for biomedical application, heating efficiency should be improved [75]. Heat dissipation of the superparamagnetic Chitosan-$MnFe_2O_4$ nanoparticles during MHT is ordinarily associated with Néel–Brownian relaxation in the frequency range suitable for hyperthermia treatment [76, 77]. The Néel–Brownian relaxation could be principally responsible for saturation behaviors (figure 5), in that the limited generation of the volumetric energy could cause the applied thermal input to be finally balanced with conductive and convective heat transfer to the surrounding area. To perform MHT, it is important to quantify an accurate SAR value. In the case of a non-adiabatic system for MHT, which can be used for convenient and reliable SAR measurement, the sample involves heat transfer between the magnetic nanoparticles and their surroundings. Therefore, it is difficult to determine an SAR value with a higher accuracy in non-adiabatic conditions. Recently, many studies about measuring SAR with experimental considerations have been reported [51, 52, 78, 79]. Although the same concentration of magnetic hyperthermia agents were applied, therapeutic temperatures could be affected by the surrounding environments due to different heat capacities and heat loss in non-adiabatic conditions [80]. Thus, it is often difficult to predict the exact therapeutic temperature. To overcome this limitation, in this study, we controlled the AC amplitudes to precisely regulate the desirable therapeutic temperature. After reaching the target temperature (i.e., 42 and 52 °C), the cell suspension maintained the target temperature within ±0.5 °C and then showed thermal equilibrium with the surrounding area until the externally-applied AC magnetic field was no longer applied (figure 9). Since SAR is dependent upon the property of MNPs and cancerous tissue characteristics, further investigations are underway to regulate chitosan-coated MNPs to achieve the optimum conditions for more effective and safer MHT *in vivo*.

4.6. Effective apoptotic cell death induced by MHT

MHT can induce diverse cancer cell death such as apoptosis or necrosis that is dependent on the exposure temperature

[81–83]. Typically, apoptotic cells with no inflammatory damage represent variations in nuclear morphology, including chromatin condensation and fragmentation, overall cell shrinkage, and blebbing of the plasma membrane in nuclear or cytoplasmic materials [84]. Thus, morphological changes were clearly visualized by an optical microscope (figure 10). As shown in figure 10(d), cellular responses after MHT at 42 °C evidently indicated cytoskeletal disintegration and genomic fragments in the cells. As MHT with Chitosan-$MnFe_2O_4$ nanoparticles sustained the temperature at the therapeutic level (~42 °C), the disrupted cytoskeleton and nucleus of the cancer cells eventually led to irreversible cell death. In fact, cleavage and disruption of the actin cytoskeleton have been observed in many other cases of apoptosis [85–88]. It is conceivable that the disruption of the cytoskeletons of the treated cells with MNPs under an AC magnetic field could be the initial indication of the apoptotic cell death. In contrast to the apoptosis, necrosis (MHT-52) occurred as a result of thermal injury, which was characterized by increased cell volume and the swelling of organelles. Due to the loss of intracellular contents, necrotic cell death can also cause significant inflammatory damage to the surrounding cells. Therefore, MHT at 42 °C exhibited the induction of effective apoptotic cell death, whereas MHT at 52 °C induced direct necrotic cell death without any apoptosis process.

According to figures 11 and 12, overheating may lead to serious clinical problems for patients. To avoid overheating, the optimal therapeutic temperature is required for effective induction of apoptosis. The current MHT settings with 1.5 mg magnetic atoms/ml of Chitosan-$MnFe_2O_4$ nanoparticles clearly generated the optimum therapeutic temperature at around 42 °C and thus induced apoptotic death for a significant number of cells. In particular, it was noted that a mere 1.5 mg magnetic atoms/ml of Chitosan-$MnFe_2O_4$ nanoparticles entailed apoptosis without injury to the peripheral normal cells by delivering the appropriate heating temperature to the targeted tumor. Thus, *in vitro* results confirmed that due to high biocompatibility and heat capacity, the Chitosan-$MnFe_2O_4$ nanoparticles could be a feasible nanomediator for effective MHT on MDA-MB-231 cancer cells. Future studies will focus on developing and evaluating biocompatible magnetic nanoprobes that can be utilized as a multimodal theranostic agent integrating therapeutics such as drug delivery and magnetic hyperthermia with optical diagnostics such as photoacoustic (PA) imaging *in vivo*. Reportedly, local hyperthermia has been shown to be effective when combined with chemotherapy or radiation therapy for cancers [89]. The induced-heat during hyperthermia can increase blood flow and oxygenation within tumors. In addition, the induced-heat during magnetic hyperthermia can trigger the drug-release from drug bioconjugated-nanoparticles. As a result, hyperthermia combined with chemotherapy and radiotherapy can increase cell sensitivity to radiation and medication and in essence, yield multiple synergistic effects. Furthermore, PA tomography is capable of providing structural and functional information in cell and tissue. In particular, PA tomography can be a promising tool to monitor the temperature within the range for hyperthermia therapy [90]. Based upon real-time PA mapping, the temperature distribution during hyperthermia can be monitored to sustain the optimal therapeutic temperature. Ultimately, multifunctional nanoparticles integrated with magnetic hyperthermia and optical imaging can be an effective theranostic approach for the early detection and treatment of small-sized cancer in real-time.

5. Conclusion

Chitosan-coated $MnFe_2O_4$ nanoparticles (Chitosan-$MnFe_2O_4$) were fabricated as an effective magnetic adjuvant for hyperthermic cancer therapy. Surface modifications with DMSA and chitosan yielded highly stable and water-dispersible superparamagnetic iron oxide nanocubes with minimal cytotoxic effects on cells. Chitosan-$MnFe_2O_4$ nanoparticles revealed a superior magnetic heating capability to commercial iron oxide nanoparticles (Feridex). 1.5 mg ml^{-1} of Chitosan-$MnFe_2O_4$ nanoparticles during magnetic field strength-controlled MHT delivered the appropriate therapeutic heating temperature (~42 °C) to the target cells and induced cellular death through apoptosis in association with thermal diffusion. Due to biocompatibility and high magnetic heating capability, Chitosan-$MnFe_2O_4$-combined MHT can be a safe and effective therapeutic method for various types of cancers.

Acknowledgments

This research was supported by a grant from the Marine Biotechnology Program (20150220) funded by the Ministry of Oceans and Fisheries, Republic of Korea.

References

[1] Laurent S and Mahmoudi M 2011 Superparamagnetic iron oxide nanoparticles: promises for diagnosis and treatment of cancer *Int. J. Mol. Epidemiol. Genet.* **2** 367–90

[2] Wang G, Chen G, Wei Z, Dong X and Qi M 2013 Multifunctional Fe_3O_4/graphene oxide nanocomposites for magnetic resonance imaging and drug delivery *Mater. Chem. Phys.* **141** 997–1004

[3] Wang G, Chang Y, Wang L, Wei Z, Kang J, Sang L, Dong X, Chen G, Wang H and Qi M 2013 Preparation and characterization of PVPI-coated Fe_3O_4 nanoparticles as an MRI contrast agent *J. Magn. Magn. Mater.* **340** 57–60

[4] Yeh C S, Su C H, Ho W Y, Huang C C, Chang J C, Chien Y H, Hung S T, Liau M C and Ho H Y 2013 Tumor targeting and MR imaging with lipophilic cyanine-mediated near-infrared responsive porous Gd silicate nanoparticles *Biomaterials* **34** 5677–88

[5] Hong S, Chang Y and Rhee I 2010 Chitosan-coated ferrite (Fe_3O_4) nanoparticles as a T2 contrast agent for magnetic resonance imaging *J. Korean Phys. Soc.* **56** 868–73

[6] Devkota J, Wang C, Ruiz A, Mohapatra S, Mukherjee P, Srikanth H and Phan M H 2013 Detection of low-concentration superparamagnetic nanoparticles using an integrated radio frequency magnetic biosensor *J. Appl. Phys.* **113** 104701

[7] Shen W, Schrag B D, Carter M J, Xie J, Xu C, Sun S and Xiao G 2008 Detection of DNA labeled with magnetic nanoparticles using MgO-based magnetic tunnel junction sensors *J. Appl. Phys.* **103** 07A306-1

[8] Lei Z Q *et al* 2012 Liver cancer immunoassay with magnetic nanoparticles and MgO-based magnetic tunnel junction sensors *J. Appl. Phys.* **111** 07E505-1~3

[9] Chalkidou A, Simeonidis K, Angelakeris M, Samaras T, Martinez-Boubeta C, Balcells L, Papazisis K, Dendrinou-Samara C and Kalogirou O 2011 *In vitro* application of Fe/MgO nanoparticles as magnetically mediated hyperthermia agents for cancer treatment *J. Magn. Magn. Mater.* **323** 775–80

[10] Laurent S, Dutz S, Hafeli U O and Mahmoudi M 2011 Magnetic fluid hyperthermia: focus on superparamagnetic iron oxide nanoparticles *Adv. Colloid Interface Sci.* **166** 8–23

[11] Basel M T *et al* 2012 Cell-delivered magnetic nanoparticles caused hyperthermia-mediated increased survival in a murine pancreatic cancer model *Int. J. Nanomedicine* **7** 297–306

[12] Giustini A J, Petryk A A, Cassim S M, Tate J A, Baker I and Hoopes P J 2010 Magnetic nanoparticle hyperthermia in cancer treatment *Nano Life* **1** 1–23

[13] Balivada S *et al* 2010 A/C magnetic hyperthermia of melanoma mediated by iron(0)/iron oxide core/shell magnetic nanoparticles: a mouse study *BMC Cancer* **10** 119

[14] Mohammad Hossein M and Amoli-Diva M 2012 Drug-carrying amino silane coated magnetic nanoparticles as potential vehicles for delivery of antibiotics *J. Nanomed. Nanotechol.* **3** 1000139

[15] Majeed M I, Lu Q, Yan W, Li Z, Hussain I, Tahir M N, Tremel W and Tan B 2013 Highly water-soluble magnetic iron oxide (Fe_3O_4) nanoparticles for drug delivery: enhanced *in vitro* therapeutic efficacy of doxorubicin and MION conjugates *J. Mater. Chem.* B **1** 2874

[16] Chomoucka J, Drbohlavova J, Huska D, Adam V, Kizek R and Hubalek J 2010 Magnetic nanoparticles and targeted drug delivering *Pharmacol. Res.* **62** 144–9

[17] Dorniani D, Hussein M Z, Kura A U, Fakurazi S, Shaari A H and Ahmad Z 2012 Preparation of Fe_3O_4 magnetic nanoparticles coated with gallic acid for drug delivery *Int. J. Nanomedicine* **7** 5745–56

[18] Van der Zee J 2002 Heating the patient: a promising approach? *Ann. Oncol.* **13** 1173–84

[19] Dudar T E and Jain R K 1984 Differential response of normal and tumor microcirculation to hyperthermia *Cancer Res.* **44** 605–12

[20] Lee J H, Jang J T, Choi J S, Moon S H, Noh S H, Kim J W, Kim J G, Kim I S, Park K I and Cheon J 2011 Exchange-coupled magnetic nanoparticles for efficient heat induction *Nat. Nanotechnol.* **6** 418–22

[21] Dokyoon Kim N L, Mihyun P, Byung Hyo K, Kwangjin A and Taeghwan H 2008 Synthesis of uniform ferrimagnetic magnetite nanocubes *J. Chem. Soc.* **131** 454–5

[22] Guardia P, Di Corato R, Lartigue L, Wilhelm C, Espinosa A, Garcia-Hernandez M, Gazeau F, Manna L and Pellegrino T 2012 Water-soluble iron oxide nanocubes with high values of specific absorption rate for cancer cell hyperthermia treatment *ACS Nano.* **6** 3080–91

[23] Pan C, Hu B, Li W, Sun Y, Ye H and Zeng X 2009 Novel and efficient method for immobilization and stabilization of β-d-galactosidase by covalent attachment onto magnetic Fe_3O_4–chitosan nanoparticles *J. Mol. Catal. B: Enzym.* **61** 208–15

[24] Malmiri H J, Jahanian M A G and Berenjian A 2012 Potential applications of chitosan nanoparticles as novel support in enzyme immobilization *Am. J. Biochem. Biotechnol.* **8** 203–19

[25] Li G-y, Jiang Y-r, Huang K-l, Ding P and Chen J 2008 Preparation and properties of magnetic Fe_3O_4–chitosan nanoparticles *J. Alloys Compd.* **466** 451–6

[26] Wang J J, Zeng Z W, Xiao R Z, Xie T, Zhou G L, Zhan X R and Wang S L 2011 Recent advances of chitosan nanoparticles as drug carriers *Int. J. Nanomedicine* **6** 765–74

[27] Elmore S 2007 Apoptosis: a review of programmed cell death *Toxicol. Pathol.* **35** 495–516

[28] Wang L *et al* 2012 Effect of magnetic nanoparticles on apoptosis and cell cycle induced by wogonin in Raji cells *Int. J. Nanomedicine* **7** 789–98

[29] Prasad N K, Rathinasamy K, Panda D and Bahadur D 2007 Mechanism of cell death induced by magnetic hyperthermia with nanoparticles of γ-$MnxFe_{2-x}O_3$ synthesized by a single step process *J. Mater. Chem.* **17** 5042

[30] Shouheng Sun H Z, Robinson D B, Raoux S, Rice P M and Shan X W A G L 2004 Monodisperse MFe_2O_4 (M = Fe, Co, Mn) nanoparticles *J. Am. Chem. Soc.* **126** 273–9

[31] Lee J H *et al* 2007 Artificially engineered magnetic nanoparticles for ultra-sensitive molecular imaging *Nat. Med.* **13** 95–9

[32] Kim D-H, Nikles D E and Brazel C S 2010 Synthesis and characterization of multifunctional chitosan-$MnFe_2O_4$ nanoparticles for magnetic hyperthermia and drug delivery *Materials* **3** 4051–65

[33] Randy De Palma S P, Van Bael M J, Van den Rul § H, Kristien Bonroy W L, Jules M, Gustaaf B and Guido M 2007 Silane ligand exchange to make hydrophobic superparamagnetic nanoparticles water-dispersible *Chem. Mater.* **19** 18321-1

[34] Pineda M G, Torres S, Lopez L V, Enriquez-Medrano F J, de Leon R D, Fernandez S, Saade H and Lopez R G 2014 Chitosan-coated magnetic nanoparticles prepared in one-step by precipitation in a high-aqueous phase content reverse microemulsion *Molecules* **19** 9273–87

[35] Feng Bai X Y and Wenqiang H 2004 Synthesis of narrow or monodisperse poly(divinylbenzene) microspheres by distillation−precipitation polymerization *Macromolecules* **37** 9746–52

[36] Fortin J-P, Wilhelm C, Servais J, Ménager C, Bacri J-C and Gazeau F 2007 Size-sorted anionic iron oxide nanomagnets as colloidal mediators for magnetic hyperthermia *J. Am. Chem. Soc.* **129** 2628–35

[37] Chou C-K 1990 Use of heating rate and specific absorption rate in the hyperthermia clinic *Int. J. Hyperthermia* **6** 367–70

[38] Hilger I, Hergt R and Kaiser W A 2005 Use of magnetic nanoparticle heating in the treatment of breast cancer *IEE Proc. Nanobiotechnol.* **152** 33–9

[39] Alexander Boadi Y T, Todaka T and Enokizono M 2005 Designing of suitable construction of high-frequency induction heating coil by using finite-element method *IEE Trans. Magn.* **41** 4048–50

[40] Stauffer P R, ZEEE M, Sneed P K, Hashemi H and Phillips T L 1994 Practical induction heating coil designs for clinical hyperthermia with ferromagnetic implants *IEEE Trans. Biomed. Eng.* **41** 17–28

[41] Calero M, Chiappi M, Lazaro-Carrillo A, Rodriguez M J, Chichon F J, Crosbie-Staunton K, Prina-Mello A, Volkov Y, Villanueva A and Carrascosa J L 2015 Characterization of interaction of magnetic nanoparticles with breast cancer cells *J. Nanobiotechnology* **13** 16

[42] Schlorf T, Meincke M, Kossel E, Gluer C C, Jansen O and Mentlein R 2010 Biological properties of iron oxide nanoparticles for cellular and molecular magnetic resonance imaging *Int. J. Mol. Sci.* **12** 12–23

[43] Wang Z and Cuschieri A 2013 Tumour cell labelling by magnetic nanoparticles with determination of intracellular iron content and spatial distribution of the intracellular iron *Int. J. Mol. Sci.* **14** 9111–25

[44] Sgonc R and Gruber J 1998 Apoptosis detection: an overview *Exp. Gerontol.* **33** 525–33
[45] Bilecka I, Kubli M, Amstad E and Niederberger M 2010 Simultaneous formation of ferrite nanocrystals and deposition of thin films via a microwave-assisted nonaqueous sol–gel process *J. Sol.-Gel. Sci. Techn.* **57** 313–22
[46] Nuryono Nuryono N M R, Bambang R, Wibawa Sakti S C and Shunitz T 2014 Coating of magnetite with mercapto modified rice hull ash silica in a one-pot process *SpringerPlus* **3** 1–12
[47] Osuna Y, Gregorio-Jauregui K M, Gaona-Lozano J G, de la Garza-Rodríguez I M, Ilyna A, Barriga-Castro E D, Saade H and López R G 2012 Chitosan-coated magnetic nanoparticles with low chitosan content prepared in one-step *J. Nanomaterials* **2012** 1–7
[48] Mahdavi M, Ahmad M B, Haron M J, Namvar F, Nadi B, Rahman M Z and Amin J 2013 Synthesis, surface modification and characterisation of biocompatible magnetic iron oxide nanoparticles for biomedical applications *Molecules* **18** 7533–48
[49] Ge Y, Zhang Y, Xia J, Ma M, He S, Nie F and Gu N 2009 Effect of surface charge and agglomerate degree of magnetic iron oxide nanoparticles on KB cellular uptake *in vitro* *Colloids Surf.* B **73** 294–301
[50] Shukla S, Jadaun A, Arora V, Sinha R K, Biyani N and Jain V K 2015 *In vitro* toxicity assessment of chitosan oligosaccharide coated iron oxide nanoparticles *Toxicol. Rep.* **2** 27–39
[51] Wildeboer R R, Southern P and Pankhurst Q A 2014 On the reliable measurement of specific absorption rates and intrinsic loss parameters in magnetic hyperthermia materials *J. Phys. D: Appl. Phys.* **47** 495003
[52] Teran F J, Casado C, Mikuszeit N, Salas G, Bollero A, Morales M P, Camarero J and Miranda R 2012 Accurate determination of the specific absorption rate in superparamagnetic nanoparticles under non-adiabatic conditions *Appl. Phys. Lett.* **101** 062413
[53] Kolhatkar A G, Jamison A C, Litvinov D, Willson R C and Lee T R 2013 Tuning the magnetic properties of nanoparticles *Int. J. Mol. Sci.* **14** 15977–6009
[54] Amidi M, Mastrobattista E, Jiskoot W and Hennink W E 2010 Chitosan-based delivery systems for protein therapeutics and antigens *Adv. Drug Deliv. Rev.* **62** 59–82
[55] Pereira C *et al* 2012 Superparamagnetic MFe_2O_4 (M = Fe, Co, Mn) nanoparticles: Tuning the particle size and magnetic properties through a novel one-step coprecipitation route *Chem. Mater.* **24** 1496–504
[56] Makridis A, Topouridou K, Tziomaki M, Sakellari D, Simeonidis K, Angelakeris M, Yavropoulou M P, Yovos J G and Kalogirou O 2014 *In vitro* application of Mn-ferrite nanoparticles as novel magnetic hyperthermia agents *J. Mater. Chem.* B **2** 8390–8
[57] Ferguson R M, Khandhar A P, Jonasson C, Blomgren J, Johansson C and Krishnan K M 2013 Size-dependent relaxation properties of monodisperse magnetite nanoparticles measured over seven decades of frequency by AC susceptometry *IEEE Trans. Magn.* **49** 3441–4
[58] Hrushikesh M, Joshi Y P L, Mohammed A, Prasad P V, Elise A S-S, Robert E, Thomas M and Vinayak P D 2009 Effects of shape and size of cobalt ferrite nanostructures on their MRI contrast and thermal activation *J. Phys. Chem.* **113** 17761–7
[59] Tromsdorf U I *et al* 2007 Size and surface effects on the MRI relaxivity of manganese ferrite nanoparticle contrast agents *Nano Lett.* **7** 2422–7
[60] Bakoglidis K D, Simeonidis K, Sakellari D and Stefanou G 2012 Size-dependent mechanisms in AC magnetic hyperthermia response of iron-oxide nanoparticles *IEEE Trans. Magn.* **48** 1320–3
[61] Li Z, Kawashita M, Araki N, Mistumori M and Hiraoka M 2010 Effect of particle size of magnetite nanoparticles on heat generating ability under alternating magnetic field *Bioceramics Develop. Appl.* **1** 1–4
[62] Müller R, Dutz S, Neeb A, Cato A C B and Zeisberger M 2013 Magnetic heating effect of nanoparticles with different sizes and size distributions *J. Magn. Magn. Mater.* **328** 80–5
[63] Martinez-Boubeta C *et al* 2013 Learning from nature to improve the heat generation of iron-oxide nanoparticles for magnetic hyperthermia applications *Sci. Rep.* **3** 1652
[64] Salazar-Alvarez G *et al* 2008 Cubic versus spherical magnetic nanoparticles: the role of surface anisotropy *J. Am. Chem. Soc.* **130** 13234–9
[65] Yongmei X Y D 2003 Effect of molecular structure of chitosan on protein delivery properties of chitosan nanoparticles *Int. J. Pharmaceut.* **250** 215–26
[66] El Ghandoor H, Zidan H M, Khalil M H and Ismail M I M 2012 Synthesis and some physical properties of magnetite (Fe_3O_4) nanoparticles *Int. J. Electrochem. Sci.* **7** 5734–45
[67] Fang C, Bhattarai N, Sun C and Zhang M 2009 Functionalized nanoparticles with long-term stability in biological media *Small* **5** 1637–41
[68] Mahmoudi M, Lynch I, Ejtehadi M R, Monopoli M P, Bombelli F B and Laurent S 2011 Protein-nanoparticle interactions: opportunities and challenges *Chem. Rev.* **111** 5610–37
[69] Lundqvist M, Stigler J, Elia G, Lynch I, Cedervall T and Dawson K A 2008 Nanoparticle size and surface properties determine the protein corona with possible implications for biological impacts *Proc. Natl Acad. Sci. USA* **105** 14265–70
[70] Thorat N D, Patil R M, Khot V M, Salunkhe A B, Prasad A I, Barick K C, Ningthoujam R S and Pawar S H 2013 Highly water-dispersible surface-functionalized LSMO nanoparticles for magnetic fluid hyperthermia application *New J. Chem.* **37** 2733
[71] Albanes A and Chan W C 2011 Effect of gold nanoparticle aggregation on cell uptake and toxicity *ACS Nano* **7** 5478–89
[72] Goycoolea F M, Valle-Gallego A, Stefani R, Menchicchi B, David L, Rochas C, Santander-Ortega M J and Alonso M J 2012 Chitosan-based nanocapsules: physical characterization, stability in biological media and capsaicin encapsulation *Colloid Polym. Sci.* **290** 1423–34
[73] Peppas N A, Thomas J B and McGinty J 2009 Molecular aspects of mucoadhesive carrier development for drug delivery and improved absorption *J. Biomater. Sci. Polym. Ed.* **20** 1–20
[74] Calatayud M P, Sanz B, Raffa V, Riggio C, Ibarra M R and Goya G F 2014 The effect of surface charge of functionalized Fe_3O_4 nanoparticles on protein adsorption and cell uptake *Biomaterials* **35** 6389–99
[75] Obaidat I, Issa B and Haik Y 2015 Magnetic properties of magnetic nanoparticles for efficient hyperthermia *Nanomaterials* **5** 63–89
[76] Seok-Hwan Chung A H, Liaohai C, Shouheng S, Konstantin Guslienko M G and Samuel D B 2006 Substrate-free biosensing using Brownian rotation of bio-conjugated magnetic nanoparticles *J. Magnetics* **11** 189–94
[77] Hergt R, Dutz S, Müller R and Zeisberger M 2006 Magnetic particle hyperthermia: nanoparticle magnetism and materials development for cancer therapy *J. Phys.: Condens. Matter* **18** S2919–34
[78] Baldi G, Lorenze G and Ravagli C 2009 Hyperthermic effect of magnetic nanoparticles under electromagnetic field *J. Ceram. Process Res.* **1-2** 103–9
[79] Coïsson M, Barrera G, Celegato F, Martino L, Vinai F, Martino P, Ferraro G and Tiberto P 2015 Specific absorption rate determination of magnetic nanoparticles through

hyperthermia measurements in non-adiabatic conditions *J. Magn. Magn. Mater.* (doi:10.1016/j.jmmm.2015.11.044)

[80] Ludwig R, Stapf M, Dutz S, Muller R, Teichgraber U and Hilger I 2014 Structural properties of magnetic nanoparticles determine their heating behavior—an estimation of the *in vivo* heating potential *Nanoscale Res. Lett.* **9** 602

[81] Fulda S, Gorman A M, Hori O and Samali A 2010 Cellular stress responses: cell survival and cell death *Int. J. Cell. Biol.* **2010** 214074

[82] Zhou J, Wang X, Du L, Zhao L, Lei F, Ouyang W, Zhang Y, Liao Y and Tang J 2011 Effect of hyperthermia on the apoptosis and proliferation of CaSki cells *Mol. Med. Rep.* **4** 187–91

[83] Natalia P, Matylevitch S T S, Jennifer R M, George R G, David F L, Cleon W G and Phillip D B 1998 Apoptosis and accidental cell death in cultured human keratinocytes after thermal injury *Am. J. Pathol.* **153** 567–77

[84] Nijhuis E H A, Poot A A, Feijen J and Vermes I 2007 *Cell Apoptosis and Cancer* ed A W Taylor (New York: Nova) pp 135–53

[85] Katschinski D M, Robins H I, Schad M, Frede S and Fandrey J 1999 Role of tumor necrosis factor a in hyperthermia-induced apoptosis of human leukemia cells *Cancer Res.* **59** 3404–10

[86] Shirazi F, Pontikos M A, Walsh T J, Albert N, Lewis R E and Kontoyianni D P 2013 Hyperthermia sensitizes rhizopus oryzae to posaconazole and itraconazole action through apoptosis *Antimicrob. Agents Chemother.* **57** 4360–8

[87] Xu Y *et al* 2008 Cobalt nanoparticles coated with graphitic shells as localized radio frequency absorbers for cancer therapy *Nanotechnology* **19** 435102

[88] Yin P T, Shah B P and Lee K B 2014 Combined magnetic nanoparticle-based microRNA and hyperthermia therapy to enhance apoptosis in brain cancer cells *Small* **10** 4106–12

[89] Rao W, Deng Z S and Liu J 2010 A review of hyperthermia combined with radiotherapy/chemotherapy on malignant tumors *Crit. Rev. J. Biomed. Eng.* **38** 101–16

[90] Ke H, Tai S and Wang L V 2014 Photoacoustic thermography of tissue *J. Biomed. Opt.* **19** 026003